# A Benchmark of Absolute and Relative Positioning Solutions in GNSS Denied Environments

Haiyun Yao [ID], Xinlian Liang [ID], *Senior Member, IEEE*, Ruizhi Chen [ID], Xiaochen Wang [ID], Hanwen Qi [ID], Liang Chen, and Yunsheng Wang

*Abstract*—Precise positioning is fundamental to the Internet of Things (IoT) that delivers insights into everything from large-scale business to ordinary smart life. Accurate localization and positioning in global navigation satellite system (GNSS) denied environments, such as indoor-, underground-spaces, and forests, is one of the most prosperous research fields because of the great complexity prompted by various challenging application scenarios. Different sensors, algorithms, and combinations of those have been developed in past decades, which provided a great variety of possible solutions that deliver different positioning accuracies. However, a rigorous evaluation of the positioning accuracy of different mainstream solutions is missing, mainly because of the difficulties in acquiring reliable ground truth for referencing and the lack of comparable test/application conditions. A comprehensive benchmarking was carried out in this study based on the comparisons of six solutions that consist of different combinations of five positioning technologies, i.e., 1) ultrawideband (UWB) and inertial measurement unit (IMU); 2) UWB, IMU, and camera; 3) UWB and light detection and ranging (LIDAR); 4) UWB and radio detection and ranging (RADAR); 5) IMU, camera, and LIDAR; and 6) UWB, IMU, camera and LIDAR. The five technologies, i.e., UWB, IMU, camera, RADAR, and LIDAR, were commonly regarded as those that are with high applicability, accuracy, and robustness. New anchors self-positioning algorithm and integrity monitoring algorithm were proposed to further aid the compared solutions and the benchmark. High-precision survey (millimeter)-level ground truth references were acquired at indoor and outdoor test locations and applied in the evaluations, to assist reliable quantitive benchmarks about the positioning accuracies and stabilities of the compared solutions. The strengths, limitations, and potentials of each solution were analyzed. It was revealed that all relative positioning solutions accumulate positioning errors over time. Such accumulation was of the highest significance for RADAR, followed by camera. LIDAR is presented to be the most robust solution for relative positioning. Compared to camera, LIDAR, and RADAR alone, the integration of different technologies clearly improved the performance. The tight coupling (TC) performed slightly superior to loose coupling, and the unscented Kalman filter with TC had a higher positioning accuracy in most cases.

*Index Terms*—Absolute and relative positioning (ARP), data fusion, global navigation satellite system (GNSS) denied environment, integrity monitoring (IM), Internet of Things (IoT), tight and loose coupling (LC).

## I. INTRODUCTION

ROBUST, accuratem and real-time positioning as the first step before other tasks are essential for almost all intelligent or smart services and applications in the Internet of Things (IoT) [1] and mobile geomatics [2]. Accurate and real-time positioning is the prerequisite for the successful implementation of IoT applications, such as intelligent logistics management [3], target positioning and tracking [4], autonomous vehicles and vehicle dynamic monitoring [5], [6], [7], the collaboration between unmanned vehicles and drones [8], and mobile health monitoring [9]. For example, in the application of human mobile health monitoring, a real-time and accurate positioning system can not only provide patients with in hospital navigation services and guide patients to their destinations quickly but also be an important means for hospitals to monitor patients in real time. Once an abnormal situation occurs, medical staff can take accurate measures to avoid accidents.

Specifically, positioning under the global navigation satellite system (GNSS) denied environments were confronted with many profound difficulties [10], [11] especially when the environmental perception and cognition tasks relied on real-time sensing and processing on board and/or on edge. After years of demanding efforts, the localization and positioning in GNSS denied environments achieved a stage where it could satisfy most of the applications requiring meter-level accuracy, e.g., in automated logistic services, autonomous driving, etc. However, great challenges remained when higher positioning accuracy, i.e., centimeter or even millimeter level accuracy, was required [12].

In general, technologies for positioning can be divided into two groups: first, relative positioning, such as inertial navigation system (INS) and simultaneous localization and mapping (SLAM) type of odometers, determines a location in relation to a reference location in a local coordinate system; second, absolute positioning, which fixes a location in a specific coordinate

framework, i.e., using GNSS, or using local communication technologies, such as the fifth generation (5G) mobile communication [13], wireless fidelity (Wi-Fi), Bluetooth low energy (BLE), and ultrawideband (UWB) [14], [15]. Specifically, for high-accuracy positioning (better than centimeter level) in GNSS denied environments, both relative and absolute positioning technologies have their strengths and weaknesses.

Absolute positioning technologies can be relatively stable over time, however, their signals are susceptible to interference from external factors, which may lead to large positioning deviations. The positioning accuracy of Wi-Fi and BLE is commonly limited to 2–10 m [16], [17], [18], [19]. Taking advantage of UWB short pulse interval and high time resolution can achieve centimeter-level positioning accuracy under the line-of-sight (LOS) conditions [20], [21], [22], [23], [24], [25]. However, when UWB comes to non-LOS (NLOS) conditions when the direct path between the radio transmitter and receiver is blocked, e.g., due to occlusions and interferences by external factors, the positioning accuracy of UWB typically declines sharply.

Relative positioning technologies are self-dependent, flexible, and accurate in a short span of time. However, their positioning error accumulates while the operational time extends. Optical-vision-based positioning using, e.g., a camera, which depends on detecting and matching visual features, is vulnerable to illumination changes. Its performance sharply degenerates in geometric degeneration conditions with few textures or features, e.g., in long straight tunnels and planar environments or in spaces with all-white or glass walls or empty areas. Laser-based positioning has a more intuitive 3-D representation, robust performance in low-light or textureless scenes and can capture fine details of an environment at a relatively long range. light detection and ranging (LIDAR) can achieve positioning accuracy at very high accuracy given sufficient accurate distance measurements, e.g., at a subcentimeter level using survey-level terrestrial laser scanning [26]. However, the performance of LIDAR positioning significantly deteriorates in large-scale open areas due to limited features. The millimeter wave (mmWave) radio detection and ranging (RADAR) is robust for the interference of fog, smoke, dust, and other small particles owing to the longer wavelength [27]. Thus, it is more suitable for hostile environments than the optical camera and LIDAR. Nevertheless, the density of RADAR measurements is much lower than that of LIDARs and cameras [28]. Therefore, RADAR is commonly used in target detection and obstacle avoidance [29], but not for positioning purposes.

Therefore, when high-precision localization and positioning were required, especially in GNSS denied environments, the trend is to integrate the absolute and relative positioning (ARP), so that they can be combined, and the weaknesses can be remedied. Such fusion of different technologies is commonly referred to as a hybrid positioning system (HPS), and the most popular fusion methods include filtering-based and factor graph optimization (FGO). The FGO method considers all the historical information and converts the probability expression into the nonlinear least square optimization. It requires multiple iterations to obtain the optimal solutions that

are computational complex [30]. Thus, it is difficult to meet the real-time requirements especially when the amount of positioning system data is large. In contrast, the filtering-based methods are more computationally efficient and have ease of implementation. Thus, filtering-based methods were used to achieve the HPSs in this study.

Various HPS solutions were proposed, and a more comprehensive review of different mainstream solutions is provided in Section II of this article. The greatest challenge now is that the actual performances, i.e., the applicability in different scenarios, the absolute accuracy, and the robustness of various HPSs are not yet clarified. A rigorous evaluation was missing, mainly because of the difficulties in acquiring reliable ground truth for referencing and the lack of comparable test/application conditions. Consequently, it was difficult to quantitatively evaluate different positioning solutions to understand their performance and their potential for different applications.

Previous research, as reviewed in Section II, had investigated the possibility to use HPS in different scenarios, but seldom discussed their accuracy and repeatability, thus, a proper understanding of the HPS reliability and applicability became difficult. This article compared a series of HPSs strategies to evaluate the accuracy of popular solutions. The proposed UWB and inertial measurement unit (IMU) positioning system supports a fast anchor self-positioning function, and the HPSs with an integrity monitoring (IM) function can effectively detect and eliminate outliers, thereby improving the accuracy and robustness of the positioning system. Furthermore, to the best of our knowledge, this work conducted the first study on the fusion of RADAR and UWB for positioning applications. RADAR is often used for target detection and obstacle avoidance in robotic applications. Its positioning accuracy and reliability are, however, relatively low in comparison to other vision positioning technologies. In this study, RADAR and UWB were fused in order to improve RADAR positioning accuracy. The performance and potential of RADAR positioning and corresponding HPSs were evaluated and explored in detail in indoor and outdoor scenarios in this study. Experiments were carried out using an unmanned ground vehicle (UGV) in four indoor and outdoor field test scenarios with LOS or NLOS conditions. Six HPSs were implemented based on the combination of one high-accuracy absolute positioning, i.e., UWB, and four popular relative positioning sensors, i.e., the IMU, camera, LIDAR, and RADAR. A comparative analysis was conducted to evaluate the performance of loose coupling (LC), tight coupling (TC), and semi-tight coupling (STC) algorithms in various indoor and outdoor scenarios, aiming to validate the effectiveness of the proposed positioning system architecture. High-precision references were acquired using high-performance Leica Nova TS60 total stations [31] and were applied to quantitatively evaluate positioning accuracy to reveal the strength, weakness, and potentials of the HPS solutions in GNSS denied/challenged environments. The main contributions of this benchmark include the following.

1) Quantitatively analyzed and evaluated the performance of the six HPSs through benchmarked comparisons with millimeter-level reference and individual positioning.

Explore and benchmark the accuracy and performance of popular ARP in different indoor and outdoor GNSS-denied/challenged environments.

2) Proposed a UWB anchor self-positioning algorithm that simultaneously estimates the positions of UWB anchors and tracks UWB tag at a centimeter level in real time, and overcomes the drawbacks of manually time-consuming measured anchor positions in advance.

3) Proposed an IM algorithm that effectively mitigates the adverse NLOS impacts on positioning and improves the accuracy and robustness of the positioning system.

4) Evaluated the potentials of HPSs through quantitative benchmarked comparisons under GNSS denied/challenged environments, and present a practical suggestion for sensor selection and integration in various positioning applications according to the potentials of benchmarked HPSs.

As mentioned before, a thorough review of relevant previous works was provided in Section II of this article. Sections III and IV introduced the experiments and relevant methods developed for the benchmark study. Section V presented and discussed the results of the benchmark, and the main findings were concluded in Section VI.

## II. LITERATURE REVIEW

This section summarized the principles, advantages, and disadvantages of the ARP technologies applied in this article, and then elaborates on previous research and common algorithms used in HPSs positioning and navigation, including sensor fusion, anchor self-positioning, and the mitigation of UWB NLOS effects. The review work also revealed that most previous studies lacked a rigorous evaluation of positioning results, e.g., only relevant tests were carried out [32], [33], [34] without the ground truth. Consequently, it is impossible to quantitatively evaluate the performance of the hybrid systems and fusion algorithms, and impossible to evaluate their potentials in various applications.

### A. Sensors

The principles, advantages, and disadvantages of the ARP sensors studied in this benchmark, i.e., UWB, IMU, camera, LIDAR, and mm Wave RADAR, are summarized in Table I.

### B. Methods of Sensor Fusion

Fusion can be done in both loose and TC approaches, and commonly used fusion algorithms include the linear Kalman filter [35], [36], extended Kalman filter (EKF) [21], [22], [24], [37], [38], [39], [40], [41], unscented Kalman filter (UKF) [21], [23], [25], [42], and particle filter (PF) [43], [44], [45].

The LC fuses the positioning results of each positioning subsystem to obtain the final positioning results. The TC combines each subsystem's observations. One advantage of TC is that it uses the raw data of each subsystem to suppress the negative impacts on positioning accuracy, even in a situation that one subsystem positioning does not work at all. For instance, when IMU and UWB are used in 3-D positioning, TC works when only one UWB range measurement is available, while LC requires at least three UWB range measurements. However, if the TC algorithm crashes, e.g., due to filter divergence, the positioning will completely fail. In contrast, one can get the positioning result from subsystem results even if the LC program does not work. In theory, the accuracy of TC could be better than that of LC as the TC employs raw measurements in nonlinear problems. In addition, the STC fuses the raw data and subsystem positioning results to obtain the final positioning result.

Linear Kalman filtering typically gives low accuracy or even divergence since the fusion models are generally nonlinear. The PF algorithms are based on the Monte Carlo method, which uses a large number of particles to simulate the state of the system and estimate the probability density function of the measurement model [45]. This method obtains higher positioning accuracy when a large number of particles are deployed, but has high computational complexity and is not optimal for systems requiring real-time positioning. The EKF approximates linearization by performing a Taylor first-order expansion for nonlinear models. It is effective when models are slightly nonlinear, but gives large truncation errors when a model is highly nonlinear. UKF uses an unscented transformation [unscented transform (UT)] on the nonlinear model instead of the Taylor expansion to generate a series of particles to simulate the posterior probability density functions of the system state and measure models. UKF does not ignore higher-order terms, which effectively overcomes the shortcomings of EKF. Its estimates are at least equivalent to the precision of the second-order Taylor expansion of nonlinear models [46] while the computational complexity of the UKF is much lower than that of the PF.

### C. Integration of Absolute and Relative Positioning Technologies

The UWB-IMU fusion has been studied in recent years [20], [22], [23], [24], [25], [35], [36], [37], [38], [39], [41], [42], [45], [47], [48], [49], [50]. The fusion of UWB and IMU reduces the IMU accumulated error [20] and improves the system's reliability and accuracy [20], [40], [51]. In NLOS environments, the fusion positioning accuracy of UWB and IMU reached centimeter level [22], [24].

Both EKF and UKF have been used in the fusion, e.g., in [20], [21], [22], [24], [39], [41] and [21], [23], [25], [42], respectively. Feng et al. [42] and You et al. [25] reported loosely coupled cases using EKF and UKF, respectively, which showed the UWB-IMU fusion could reach a centimeter-level accuracy in LOS environments.

Hybrid UWB-vision systems were reported to have higher accuracy than individual systems [52], [53], [54], [55], [56]. The UWB-vision fusion was reported for UAVs [52], [54] and pedestrian [55] positioning. Extra stationary markers with known positions were required, e.g., in [52]. The UWB and UWB-vision positioning accuracies were around 0.300 and 0.200 m, respectively [55]. A tightly coupled UWB-aided monocular visual SLAM system in [56] achieved positioning

TABLE I
PRINCIPLE, ADVANTAGES, AND DISADVANTAGES OF ARP SENSORS

| Sensors | Principle | Advantage | Disadvantage |
|---|---|---|---|
| UWB | High accuracy positioning through precise ranging. | • Provide absolute position;<br>• High-precision ranging;<br>• Low-power;<br>• Cost is reducing, being used in consumer devices. | • Require extra infrastructure (Anchors must be set in advance);<br>• Problems inherent to wireless signals (Like multipath and NLOS) |
| IMU | Measure angular rate and specific force to derive motion states (e.g., attitude, velocity, and position, etc.). | • Self-contained;<br>• Full motion states;<br>• High accuracy in a short time;<br>• High update frequency, such as up to 200Hz or higher;<br>• Low-cost IMU as the off-the-shelf sensors are embedded in consumer-grade products. | • High cost of a high-performance IMU;<br>• Significant drift errors for low-cost IMU;<br>• Bias in IMU components such as accelerometers and gyroscopes. |
| Camera | Detect and match visual features to derive position and mapping. | • Low cost compares to LIDAR and RADAR;<br>• Rich feature information and color information;<br>• Passive sensing technology is immune to the effects of wireless signal propagation errors like the NLOS. | • Vulnerable to weather and illumination conditions and its performance degrades under harsher conditions, such as in darkness, rain, fog, and snow;<br>• The amount of raw camera data is large. |
| LIDAR | Use infrared light waves to measure distances and generate point clouds. | • High-precision ranging and data density;<br>• Robust to low-light or texture-less scenes;<br>• More intuitive map representation;<br>• Capture fine details of an environment at long ranges. | • High cost of a high-performance LIDAR;<br>• Dependency on the significance of features;<br>• The performance of positioning and mapping significantly deteriorates in open areas. |
| RADAR | Emit radio waves for ranging, object detection and obstacle avoidance. | • All-weather applications;<br>• Low cost compares to LIDAR;<br>• Further measurement range compare to LIDAR;<br>• Robust for the interference of fog, smoke, and dust. | • Low measurement density;<br>• Cannot detect markers. |

accuracies at around 3.000 m using monocular vision and about 0.400 m using the UWB-aided visual SLAM in an open area. The UWB, monocular vision, and their combination got 0.300, 1.000, and 0.250 m positioning accuracies, respectively, in a rectangular open space [53].

The UWB-LIDAR fusion not only improved the UWB positioning accuracy but also removed the accumulated error in the LIDAR SLAM algorithm, which suits infrastructure-less and ad-hoc applications without prior environment information. Major challenges exist in geometric degeneration scenes, such as long straight tunnels and planar environments, where the reliability of LIDAR-tracked features drops sharply. Song et al. [32] studied the UWB-LIDAR fusion in a 2-D SLAM. For achieving robust localization in geometrically degenerated environments like the tunnels, Zhen and Scherer [33] presented a degeneration characterization model using UWB and LIDAR to estimate the positioning performance at a given location in a prior map and combined IMU, LIDAR, and UWB based on a probabilistic sensor fusion method. Zhou et al. [34] used EKF to fuse UWB and LIDAR loosely in a geometric degeneration environment. The results showed that it might not be able to provide reliable positioning accuracy in the UWB NLOS environment.

The mmWave RADAR received extensive attention due to its ability to work effectively in harsh environments. However, since mmWave RADAR has low cross-range resolution and

sparse measurements [57], it often needs to be fused with other sensors for better performance. There are few studies on the use of RADAR for positioning, especially the research on fusion with absolute positioning sensors. Tan et al. [58] applied 5G mobile communication and mmWave RADAR to air traffic management, where RADAR was used for target detection and recognition. Yao et al. [59] presented a TC study of UWB and mmWave RADAR in an indoor environment based on EKF. The average positioning accuracies of RADAR and fusion were around 0.770 and 0.320 m, respectively. In addition, the RADAR-IMU fusion was reported to achieve the positioning of the ground robot [27] and ego-velocity estimation in visually degraded environments [60], RADAR-IMU fusion reached positioning accuracy at around 1.000 m. In [57], the fusion of the monocular camera and mmWave RADAR used a trained deep neural network and long short-term memory (LSTM) approach to realize target tracking.

### D. Anchor Self-Positioning

Anchor positions are manually measured in advance as prior information in most UWB-based positioning solutions [20], [21], [22], [23], [24], [25], [39], [41] to locate the UWB tag. Manually measuring anchor positions requires extra measuring tools, such as a laser meter and is time-consuming and labor-intensive. It is not suitable for emergency applications where the place is inaccessible or dangerous, such as areas with harmful gas or high radiation, or the task is time critical, such as disaster rescue and firefighting, or the anchor positions change during the positioning process, such as the cooperative positioning of multiple drones or unmanned vehicles.

Anchor self-positioning was studied in [43], [45], [48], [50], [56], [61], [62], [63], and [64]. The realization of the anchor self-positioning function reduced the error caused by the manual measurement of the anchor position and improved the efficiency. Tian et al. [45] used UWB and pedestrian dead reckoning (PDR) based on multilateration to achieve anchor self-positioning in post-processing, which is not suitable for positioning anchors in scenarios where the anchors need to move. The results showed decimeter-level anchors positioning for only one anchor. Centimeter-level anchor positioning using simulation data was reported in [50]. Hamer and D'Andrea [48] reported a centimeter-level UWB anchor self-positioning based on multiple micro-unmanned aerial vehicle platforms. It required communication between anchors to calculate the distance between them, and clock synchronization and additional hardware communication to calculate the time difference of arrival (TDOA). Nguyen et al. [64] reported a geometric method to calculate anchor coordinates, given known distances between anchors.

Anchors self-positioning function of some other positioning sensors was presented in [43], [61], and [62]. In [56] and [63], the bundle adjustment method was used to fuse the camera, IMU, and UWB, and the centimeter-level UWB anchor position was estimated based on the visual-inertial derivative combined with the UWB pseudo ranges (PRs). Esslinger et al. [62] used the optoacoustic sensor and the IMU to achieve centimeter-level anchor positioning, but the transmitter requires four optoacoustic sensors. Lee et al. [43] used the IMU and 802.15.4a chirp spread spectrum (CSS) radio for beacon self-positioning based on particle filtering. The average value of the particles is used as the position of the beacon when the particles converge. The position accuracy of the beacon is at the meter level, and the calculation complexity is high due to the use of particle filtering.

### E. UWB NLOS Identification and Mitigation

A common factor that affects the UWB positioning accuracy is the NLOS radio propagation. Research has been carried out to identify, mitigate, or eliminate the NLOS impacts on UWB positioning [49], [65], [66], [67], [68], [69], [70].

Zhang et al. [68] proposed an NLOS identification method based on UWB PR and an empirical threshold. The report showed that the method improved UWB positioning accuracy, given redundant PRs existed. Nevertheless, using only the PRs to identify the NLOS cannot eliminate the impact of the NLOS when the given empirical threshold is inaccurate. Li and Wang [70] used a factor graph method to alleviate NLOS, which is highly computationally complicated.

Machine learning and deep learning have been studied in recent years in NLOS identification [49], [65], [66], [67], [69]. Yu et al. [49] proposed a fuzzy comprehensive evaluation method for NLOS identification in complex environments. This method was reported to be able to effectively identify NLOS. Support vector machines (SVM) were reported to be able to effectively identify NLOS [65], [66], [67]. Zeng et al. [67] identified NLOS using SVM by training channel impulse response (CIR) data, this method can effectively identify NLOS, given a suitable kernel function. Jiang et al. [69] used deep learning to identify NLOS based on convolutional neural network (CNN) and LSTM, using CNN-LSTM to train UWB CIR offline data. Machine learning or deep learning requires offline data learning and training. Insufficient offline data will lead to under- or over-fitting problems in model training.

## III. DESIGN OF SYSTEM AND EXPERIMENTS

This section presents the experiment platform, sensors, and test setups used in the tests.

### A. Platform and Sensors

The equipment used in the experiment is shown in Fig. 1. The mobile platform was the SCOUT mini model UGV (AgileX Robotics, Shenzhen, China). The positioning sensors included a set of LinkTrack P-B UWB devices (NoopLoop Technology Company, Ltd., Shenzhen, China), a RealSense Tracking Camera T265 (Intel, Santa Clara, CA, USA), a PandarXT-32 laser LiDAR (Hesai Technology, Shanghai, China), an Eagle mmWave RADAR (Oculii, Dayton, OH, USA). The onboard computing unit was an Intel NUC computer (Intel, Santa Clara, CA, USA).

The LiDAR had a 0.5-centimeter (cm) ranging accuracy, a 120-m measuring range, a 360°/31° horizontal/elevational field of view (FOV), and a 0.18° horizontal angular resolution, and a 10-Hz scan rate at 32 lines/sec. The RADAR
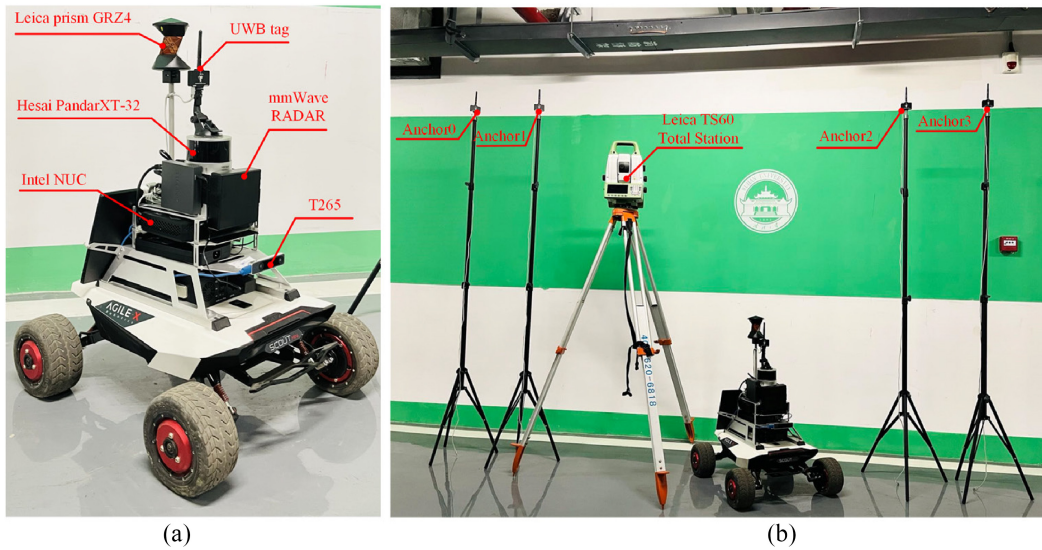
Fig. 1.　Experiment equipment. (a) Multisensors positioning platform. (b) Total station and UWB anchors.

TABLE II
EXPERIMENT SITES AND SETUP

| | Indoor | | | | Outdoor | | | |
|---|---|---|---|---|---|---|---|---|
| **Sites** | **Meeting Room** | | **Underground Parking** | | **Library Square** | | **Basketball Court** | |
| **Snapshot** |  | |  | |  | |  | |
| **Description** | Many tables and chairs. With some NLOS. | | Relatively empty. | | Empty, surrounding objects, e.g. walls, trees., etc. | | Empty, objects on one side. | |
| **Notation [a]** | Indoor I-1 | Indoor I-3 | Indoor II-1 | Indoor II-3 | Outdoor I | Outdoor II | Outdoor III-1 | Outdoor III-3 |
| **Size of tested area (m²)** | 10×10 | | 13×7 | | 17×17 | | 15×15 | |
| **The lengths of the Ground Truth (m)** | 28.4 | 84.8 | 28.3 | 83.7 | Outdoor I-1　52.4　Outdoor I-3　156.2 | Outdoor II-1　51.8　Outdoor II-3　155.5 | 46.3 | 139.4 |
| **Ground truth trajectories** |  | | | | | | | |

[a] The letter "I, II, III" denotes the site numbers; Numbers "1" and "3" mean the site was covered by 1 and 3 trajectories, respectively.

had a 0.86-m ranging accuracy, a 400-m measuring range, a 120°/45° horizontal/elevational FOV, <1° horizontal angular resolution, and a 15-Hz scan rate. The UWB had a tag and four anchors. The T265 camera includes two fisheye lens sensors with a combined 163° FOV (+/− 5°). The UWB tags and T265 camera all have low-cost MEMS-IMU. The UWB tag has MPU-6500 (InvenSense Company, San Jose, CA, USA), and the T265 has BMI055 (BOSCH Company, Stuttgart, Germany). Their detailed specifications can be found in [71] and [72].

The reference trajectories, or the ground truths, were collected using a Leica TS60 total station and a GRZ4 360° prism (Leica, Heerbrugg, Switzerland) fixed on the UGV. The GRZ4 360° prism delivers an overall accuracy of 2–5 mm and an automatic target recognition of up to 600 m [73].

## B. Experiment Setup

The performances of the ARP solutions were evaluated and compared in four indoor and outdoor experimental scenes in this article. In each experiment, a roughly repeated route was gone through three times. Single and repeated routes were compared, to evaluate the drifting effects over time of the relative positioning, i.e., IMU, camera, LIDAR, and RADAR.

Table II summarized experimental scenes and their ground truth. The experiments were numbered according to the site and trajectory number. For instance, the experiments in the indoor meeting room with single and repeated trajectories were named Indoors I-1 and I-3, respectively.

## C. UWB Sensor Networks

In absolute positioning, the positioning accuracy is affected by both the algorithm and geometry of UWB sensor networks, similar to the satellite constellation. The dilution of precision (DOP), an indicator of satellite geometry for the satellite constellation, was used to evaluate the network configuration. The 2-D plane positioning accuracy within the UWB networks was simulated to reveal the impacts of the geometry of UWB networks, i.e., the horizontal DOP (HDOP). A smaller HDOP value represents a more optimal geometry of sensor networks for positioning. The method detailed for calculating HDOP can be found in the previous work [18], [74]. Readers are referred to Appendix A for the simulated result of the HDOP in four experimental scenes.

## IV. Algorithms and Solutions in the Benchmarking

This section presents the six HPS solutions that were benchmarked in this study. Moreover, different methods for the fusion of technologies in each HPS solution were also studied. Two new algorithms, i.e., one for anchor self-positioning, and one for IM, were introduced to improve the state of the art of positioning accuracy of relevant HPS solutions. Technical and algorithm details are presented in this section to support an in depth and convenient understanding of the benchmarked solutions.

## A. Overview of Six Benchmarked HPS Solutions

HPS-1 integrates UWB and IMU, and four fusion methods, i.e., EKF-LC, EKF-TC, UKF-LC, and UKF-TC, were compared to analyze their performances. The UKF fusion algorithm was tested only in HPS-1 because the state models of HPS-2, -3, and -4 and the measurement model of HPS-5 are linear. The integration between UWB and CAMERA in HPS-2, and HPS-3, as well as between LIDAR and RADAR in HPS-4 are carried out using EKF-TC, to study the performances of different combinations of the relative and absolute positioning. HPS-5 evaluated only the relative positioning performance, i.e., IMU, CAMERA, and LIDAR, based on EKF-LC. HPS-6 tested the performance of multiple positioning subsystems based on STC, i.e., when UWB, IMU, CAMERA, and LIDAR are all combined.

In the experiments, the strap-down inertial navigation system (SINS) [75], [76], [77], [78] used IMU positioning,

TABLE III
DETAILED INFORMATION OF THE SIX HPSs

| HPSs | | Fusion Engines | Relative Positioning Algorithms | Integrity Monitoring |
|---|---|---|---|---|
| 1 | UWB-IMU | EKF-LC | SINS | IBIM |
| | | UKF-LC | | |
| | | EKF-TC | | PROD, IBIM |
| | | UKF-TC | | |
| 2 | UWB-CAMERA-IMU | EKF-TC | ORB-SLAM3 | PROD, IBIM |
| 3 | UWB-LiDAR | | A-LOAM | |
| 4 | UWB-RADAR | | | |
| 5 | IMU-CAMERA-LiDAR | EKF-LC | SINS, ORB-SLAM3, A-LOAM | IBIM |
| 6 | UWB-IMU-CAMERA-LiDAR | EKF-STC | | PROD, IBIM |

the ORB-SLAM3 algorithm [79] in a stereo-inertial mode used CAMERA positioning, and the A-LOAM algorithm [80] was used for LIDAR and RADAR positioning.

A new IM algorithm was proposed to tackle the negative impacts of UWB-NLOS, which integrates PRs outlier detection (PROD) and innovation-based integrity monitoring (IBIM) phases for the detection of measurement outliers caused by radio NLOS propagation, thus, further improving the precision and robustness of the positioning system.

Table III summarizes the fusion engines, the relative positioning algorithms, and the IM algorithms of the six benchmarked HPSs.

The structures of the six HPSs are illustrated in block diagrams in Figs. 2–5.

HPS-1 included both TC and LC, where TC is shown in Fig. 2 as an example. The pseudo ranges between the UWB anchors and tag were based on the time of flight (TOF). The outliers of pseudo ranges affected by NLOS were eliminated in the IM, and the filtered pseudo ranges were input into the fusion engine. The anchor positions were estimated by the proposed UWB anchor self-positioning algorithm in real time (see Section IV-E). In the IMU positioning subsystem, the real-time position, velocity, and attitude (PVA) were obtained by the SINS algorithm given initial IMU PVA, acceleration, and gyroscope zero bias. The ranges between the anchors and IMU can be estimated using anchor and IMU positions in real time.

In the fusion engine, the discrete-time error state space the model was given based on the SINS algorithm. The system measurement model referred to the difference between the estimated ranges from the UWB anchor positions to the IMU position and pseudo ranges calculated by the UWB. The proposed IBIM further improved the accuracy and robustness of the positioning system by further removing measurement outliers. The real-time estimated state vector error (PVA error, acceleration, gyroscope zero bias, and anchors error) was then
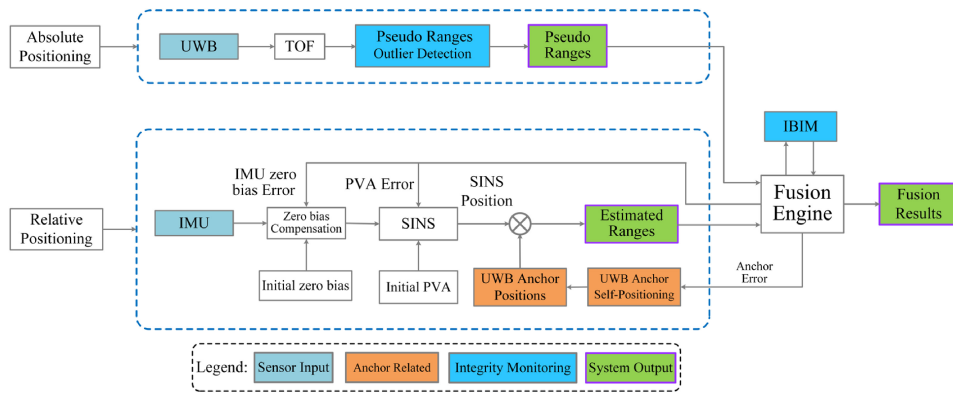
Fig. 2.   Block diagram of the HPS-1 based on the tightly couple.
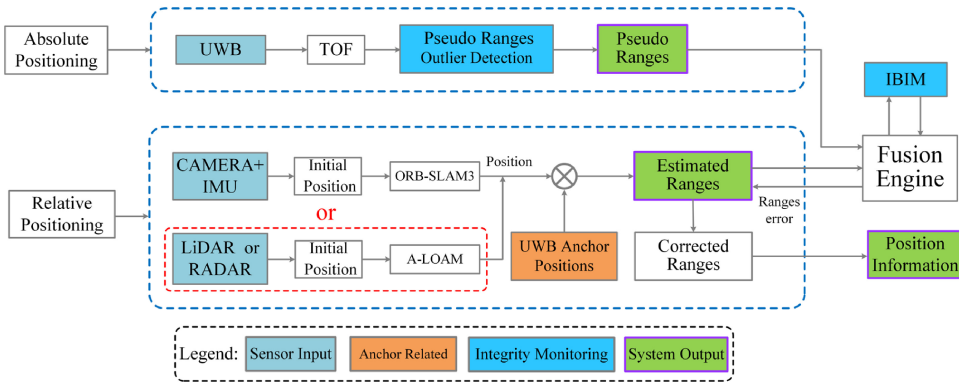


Fig. 3.   Block diagram of the HPS-2 (UWB+CAMERA+IMU), HPS-3 (UWB+LiDAR), and HPS-4 (UWB+RADAR) based on TC.
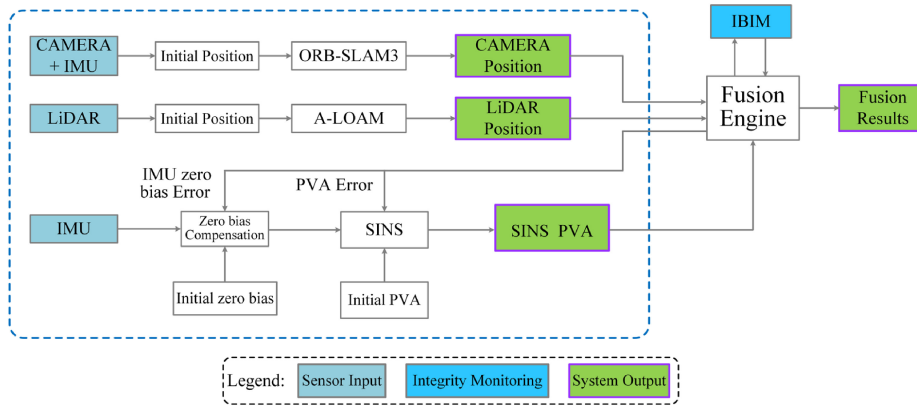


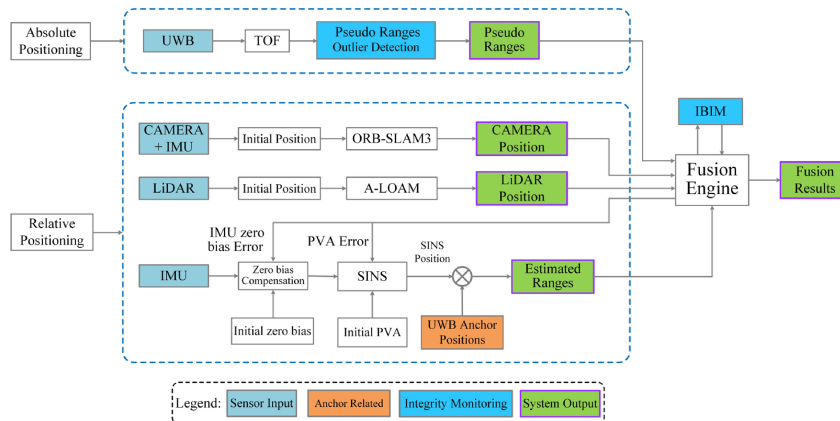Fig. 4.   Block diagram of the HPS-5 based on the LC.



Fig. 5.   Block diagram of the HPS-6 based on the STC.

feedback to the SINS and UWB anchors position estimation. The final fusion result was obtained through the error feedback correction.

HPS-2, -3, and -4 integrated the absolute positioning subsystem UWB and the relative positioning subsystem camera-IMU, LIDAR, and RADAR, respectively. The system error state model refers to the distance error between UWB anchors and the tag. The system measurement model refers to the difference between the estimated ranges inferred by the relative position subsystem and pseudo ranges calculated by the absolute position subsystem. The optimal state estimate after filtering would feedback to the estimated range between the UWB anchors and relative positioning sensors (i.e., CAMERA, LIDAR, and RADAR) as shown in Fig. 3. The corrected range estimation was used to solve the final position information by the least square.

HPS-5 combined three relative positioning sensors, i.e., IMU, CAMERA, and LIDAR, as shown in Fig. 4. The system state model was the same as that of HPS-1. The system measurement model referred to the difference between CAMERA and IMU positions, and the LIDAR and IMU positions. The proposed IBIM was performed to improve the accuracy as well as the robustness of the positioning system. The real-time estimated state vector errors were feedbacked to the SINS and the fusion results were obtained through the error feedback correction.

HPS-6 combined all ARP sensors as shown in Fig. 5. HPS-6 added two relative positioning of CAMERA and LIDAR in addition to HPS-1. To compensate for the shortcomings of the tight and loose coupling, the fusion engine adopts a semi-tight couple method. In the fusion engine, the system state model was the same as that of HPS-1. The system measurement model was divided into two parts. The first part was the difference between the estimated range from the UWB anchors positions to the IMU position and pseudo ranges calculated by the absolute position subsystem. The second part was the difference between the position of the camera and the position of the IMU and the position difference between the position of the LIDAR and the IMU. The proposed IM detects outliers in real time. The real-time estimated state vector errors were feedbacked to the SINS and the fusion results will be obtained through the error feedback correction.

### B. Relative Positioning Based on IMU Sensor

The SINS algorithm was based on the classical Newtonian mechanical theory, using the specific force $f$ and angular rate $\omega$ integral provided by the IMU accelerometer and gyroscope to calculate the object PVA [76], [81]. The PVA of the SINS update algorithm was as follows [75], [76], [77], [78]:

$$
\begin{cases}
\boldsymbol{q}_{b(k)}^{n(k)} = \boldsymbol{q}_{b(k-1)}^{n(k-1)} \otimes \boldsymbol{q}_{b(k)}^{b(k-1)} \\
\boldsymbol{v}_k^n = \boldsymbol{v}_{k-1}^n + \Delta \boldsymbol{v}_{f,k}^n + \Delta \boldsymbol{v}_{g/cor,k}^n \\
\boldsymbol{\rho}_k^n = \boldsymbol{\rho}_{k-1}^n + \frac{1}{2}\left(\boldsymbol{v}_k^n + \boldsymbol{v}_{k-1}^n\right)dt
\end{cases}
\tag{1}
$$

$$
\boldsymbol{q}_{b(k)}^{b(k-1)} = \begin{bmatrix} \cos\|0.5\phi_k\| \\ \frac{\sin\|0.5\phi_k\|}{\|\phi_k\|}\phi_k \end{bmatrix}
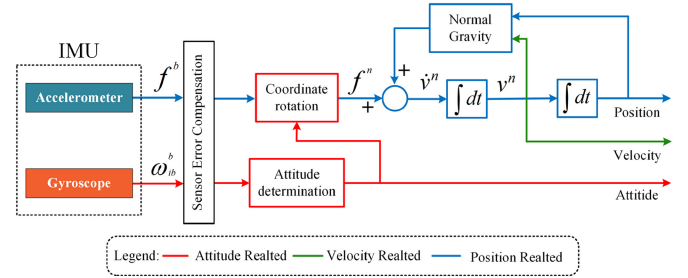\tag{2}
$$



Fig. 6. Conceptual diagram of an INS.

where $\boldsymbol{q}_{b(k)}^{n(k)}$ is the unit quaternion representing the rotation from the body frame (i.e., $b$ frame) to the navigation frame (i.e., $n$ frame) at the $k$ moment. The notation $\otimes$ represents the quaternion multiply, the $\phi_k$ is the equivalent rotation vector of the $b$ frame from the time $k$ to $k$-1 [78]. $\boldsymbol{v}_k^n$ and $\boldsymbol{v}_{k-1}^n$ are the velocity of the $n$ frame at the time $k$ and $k-1$, respectively. $dt$ is the IMU sampling interval. $\Delta \boldsymbol{v}_{f,k}^n$ is the specific force velocity increment. $\Delta \boldsymbol{v}_{g/cor,k}^n$ is the velocity increment caused by gravity and Coriolis force. $\boldsymbol{\rho}_k^n$ is the position of the $n$ frame at the $k$ time. A detailed derivation of the SINS algorithm can be found in [75], [76], [78], [81], and [82]. The conceptual diagram of a SINS is shown in Fig. 6.

The $\boldsymbol{f}^n = \mathbf{C}_b^n \boldsymbol{f}^b$ is the specific force in the frame $n$ in Fig. 6, $\mathbf{C}_b^n$ is the corresponding rotation matrix of the $\boldsymbol{q}_b^n$, $\boldsymbol{\omega}_{ib}^b$ is the angular rate of the body frame, and $\dot{\boldsymbol{v}}^n$ is the velocity differentiation or the body motion acceleration in the frame $n$. When the motion acceleration $\dot{\boldsymbol{v}}^n$ is accurately estimated, the velocity can be calculated by integrating the $\dot{\boldsymbol{v}}^n$, and the position can be obtained by integrating again.

The system discrete-time error state-space model based on the SINS update algorithm can be derived according to the standard additive error definition for the PVA, and accelerometer and gyroscope biases ($\hat{x} \cong x + \delta x$). Discrete-time error state-space model at the $k$ time can be described as follows when the SINS sampling interval $dt$ [83], [84]:

$$
\begin{cases}
\delta\boldsymbol{\rho}_{k+1}^n = \delta\boldsymbol{\rho}_k^n + dt\delta\boldsymbol{v}_k^n \\
\delta\boldsymbol{v}_{k+1}^n = \delta\boldsymbol{v}_k^n + dt\left[\mathbf{C}_{b,k}^n \boldsymbol{f}_k^b\right]^\times \delta\boldsymbol{\varphi}_k^n + dt\mathbf{C}_{b,k}^n\left(\delta\boldsymbol{b}_{a,k} + \boldsymbol{n}_{f,k}\right) \\
\delta\boldsymbol{\varphi}_{k+1}^n = \delta\boldsymbol{\varphi}_k^n - dt\mathbf{C}_{b,k}^n\left(\delta\boldsymbol{b}_{g,k} + \boldsymbol{n}_{\omega,k}\right) \\
\delta\boldsymbol{b}_{a,k+1} = \delta\boldsymbol{b}_{a,k} + dt\boldsymbol{n}_{\delta f,k} \\
\delta\boldsymbol{b}_{g,k+1} = \delta\boldsymbol{b}_{g,k} + dt\boldsymbol{n}_{\delta\omega,k}
\end{cases}
\tag{3}
$$

where $\boldsymbol{\rho}$, $\boldsymbol{v}$, $\boldsymbol{\varphi}$, $\boldsymbol{b}_a$, and $\boldsymbol{b}_g$ are the PVA, accelerometer biases, and gyroscope biases. $[\bullet]^\times$ denotes the skew-symmetric matrix representation of the cross-product operation. The $n_{\delta f}$ and $n_{\delta\omega}$ are the accelerometer and gyroscope bias increments, respectively, which are modeled as white Gaussian noises. $\boldsymbol{n}_f$ and $\boldsymbol{n}_\omega$ are temporally uncorrelated zero-mean noise processes of the accelerometer and gyroscope, respectively.

### C. Absolute Positioning Based on UWB Sensor

The PR between the UWB anchors and the tag was commonly calculated by the time of arrival (TOA) [85], [86], [87], the TDOA [87], [88], and TOF [50], [89]. The TOA required clock synchronization for anchors and tags. TDOA required clock synchronization only for the anchors. The TOF did not
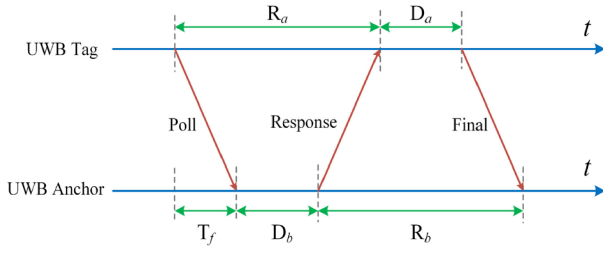
Fig. 7.   DS-TWR exchange.

require clock synchronization. It was calculated by the Double-sided two-way ranging (DS-TWR) method [89] and was used to solve the PR in the experiment. Fig. 7 shows a DS-TWR exchange.

According to Fig. 7, the round-trip time from the tag sending a poll message to receiving the response message from the anchor $R_a$, and the round-trip time from the anchor sending a response message to receiving the final message from a tag $R_b$ can be expressed as follows:

$$\begin{cases} R_a = 2T_f + D_b \\ R_b = 2T_f + D_a \end{cases} \quad (4)$$

where $T_f$ is the TOF from tag to anchor, the delays $D_a$ and $D_b$ of the tag and anchor are constants and known parameters from the hardware.

Therefore, the $T_f$ between tag and anchor can be calculated as follows:

$$T_f = \frac{R_a R_b - D_a D_b}{R_a + R_b + D_a + D_b}. \quad (5)$$

And, the PR $\boldsymbol{d}_m$ between tag and anchor can be written as follows:

$$\boldsymbol{d}_m = T_f \times c = \|\boldsymbol{\rho}_m^n - \boldsymbol{P}_{\text{candidates}}^n\| + \boldsymbol{\vartheta}, \boldsymbol{\vartheta} \sim N\left(0, \sigma^2\right)$$
$$(m = 1, \dots, M) \quad (6)$$

where $c$ is the speed of light; $\| \bullet \|$ is the Euclidean distance (2-norm); $\boldsymbol{\rho}_m^n$ is the 3-D coordinates of the $m$th anchor in the navigation frame $n$; $\boldsymbol{P}_{\text{candidates}}^n$ is the position of relative positioning sensors in the navigation frame $n$, which is the IMU-position estimate $\boldsymbol{P}_{\text{imu}}^n$ in HPS-1, -5, and -6, the camera-position estimate $\boldsymbol{P}_{\text{camera}}^n$ in HPS-2, the LiDAR-position estimate $\boldsymbol{P}_{\text{LiDAR}}^n$ in HPS-3, the RADAR-position estimate $\boldsymbol{P}_{\text{radar}}^n$ in HPS-4; $\boldsymbol{\vartheta}$ is the ranging error with zero-mean Gaussian normal distribution; and $M$ is the number of available anchors.

The tag position $(x, y, z)$ can be calculated by multilateration combined with the Gauss–Newton iteration [18], [90]. Details are in Appendix B.

### D. Fusion of Relative and Absolute Positioning Information

The relative and absolute positioning sensors are integrated using EKF and UKF algorithms.

Given the state and measurement models of a system

$$\begin{cases} X_k = f(X_{k-1}, \ \mu_{k-1}) + W_{k-1} \\ Z_k = h(X_k) + V_k \end{cases} \quad (7)$$

where $f$ is the nonlinear state function, $h$ is the nonlinear measurement function, $W_k$ and $V_k$ are the process and measurement noise with uncorrelated zero-mean white Gaussian noise and covariances $\mathbf{Q}_k$ and $\mathbf{R}_k$, respectively, i.e., $W_k \sim N(0, \mathbf{Q}_k)$ and $V_k \sim N(0, \mathbf{R}_k)$. The TC and LC processes of EKF and UKF for the HPSs are presented in Sections IV-D1 and IV-D2, respectively.

*1) TC and LC Based on EKF:* The main core idea of the EKF algorithm is to linearize the nonlinear state or measurement models by the Taylor series expansion and retain the first-order terms, which omit the second-order and above terms. The detailed process of the EKF algorithm can be referred to in [42].

*a) System error state models:* According to (3), the system error state model of HPS-1, -5, and -6 can be written as follows:

$$\delta X = \begin{bmatrix} \delta\boldsymbol{\rho}^T & \delta\boldsymbol{v}^T & \delta\boldsymbol{\varphi}^T & \delta\boldsymbol{b}_a^T & \delta\boldsymbol{b}_g^T \end{bmatrix}^T. \quad (8)$$

Hence, the linearized state-space system model of the discrete-time process is

$$\delta X_{k+1} = \mathbf{F}_k \delta X_k \quad (9)$$
$$\mathbf{P}_{k+1} = \mathbf{F}_k \mathbf{P}_k \mathbf{F}_k + \mathbf{G}_k \mathbf{Q}_k \mathbf{G}_k^T \quad (10)$$

where $\delta X_k$ is the error state at time $k$, $\delta X_{k+1}$ is the predicted error state vector, $\mathbf{P}_{k+1}$ is the priori covariance matrix, and $\mathbf{F}_k$ denotes the state transition matrix, $\mathbf{G}_k$ denotes the noise-driving matrix

$$\mathbf{F}_k = \begin{bmatrix} \mathbf{I} & dt\mathbf{I} & \mathbf{0} & \mathbf{0} & \mathbf{0} \\ \mathbf{0} & \mathbf{I} & dt\begin{bmatrix} \mathbf{C}_{b,k}^n \mathbf{f}_k^b \end{bmatrix}^\times & dt\mathbf{C}_{b,k}^n & \mathbf{0} \\ \mathbf{0} & \mathbf{0} & \mathbf{I} & \mathbf{0} & -dt\mathbf{C}_{b,k}^n \\ \mathbf{0} & \mathbf{0} & \mathbf{0} & \mathbf{I} & \mathbf{0} \\ \mathbf{0} & \mathbf{0} & \mathbf{0} & \mathbf{0} & \mathbf{I} \end{bmatrix}. \quad (11)$$

$$\mathbf{G}_k = \begin{bmatrix} \mathbf{0} & \mathbf{0} & \mathbf{0} & \mathbf{0} \\ dt\mathbf{C}_{b,k}^n & \mathbf{0} & \mathbf{0} & \mathbf{0} \\ \mathbf{0} & -dt\mathbf{C}_{b,k}^n & \mathbf{0} & \mathbf{0} \\ \mathbf{0} & \mathbf{0} & dt\mathbf{I} & \mathbf{0} \\ \mathbf{0} & \mathbf{0} & \mathbf{0} & dt\mathbf{I} \end{bmatrix}$$

$$\mathbf{Q}_k = \begin{bmatrix} \sigma_{\mathbf{a}_n}^2 \mathbf{I} & \mathbf{0} & \mathbf{0} & \mathbf{0} \\ \mathbf{0} & \sigma_{\omega_n}^2 \mathbf{I} & \mathbf{0} & \mathbf{0} \\ \mathbf{0} & \mathbf{0} & \sigma_{\mathbf{a}_\omega}^2 \mathbf{I} & \mathbf{0} \\ \mathbf{0} & \mathbf{0} & \mathbf{0} & \sigma_{\omega_\omega}^2 \mathbf{I} \end{bmatrix} \quad (12)$$

where $\mathbf{I}$ and $\mathbf{0}$ represent the $3 \times 3$ identity matrix and $3 \times 3$ zero matrices, respectively, the $\sigma_{\mathbf{a}_n}$ and $\sigma_{\boldsymbol{\omega}_n}$ represent the standard deviation of white Gaussian noise for acceleration and angular velocity, respectively, and $\sigma_{\mathbf{a}_\omega}$ and $\sigma_{\boldsymbol{\omega}_\omega}$ represent the standard deviation of white Gaussian noise for acceleration and angular velocity bias, respectively.

The system error state model $\delta X$ of the HPS-2, -3, and -4 are as follows:

$$\delta X = [\delta d_1 \delta d_2 \delta d_3 \delta d_4] \quad (13)$$

where the $\delta X$ denotes the distance error between the UWB tag and anchors. Since the total numbers of UWB anchors were four in this study, the state transition matrix $\mathbf{F}_k$ is the identity matrix diag $(1, 1, 1, 1)$ in the HPS-2, -3, and -4.

*b) System measurement models:* Assume the coordinates of the available UWB anchors in the navigation coordinate system are $\boldsymbol{\rho}_m^n$ ($m = 1, 2, \ldots, M$), according to (6), the measurement models of the HPS-1, -2, -3, and -4 can be expressed as follows:

$$Z_k = \|\boldsymbol{\rho}_m^n - \boldsymbol{P}_{\text{candidates}}^n\| - \boldsymbol{d}_m, m = 1, 2, \ldots, M. \quad (14)$$

By linearizing (14), the measurement equation can be written as follows:

$$Z_k = \mathbf{H}_k \delta X_k + v_k \quad (15)$$

where $\mathbf{Z}_k$ is the measurement error vector and $v_k$ is the measurement noise with the covariance matrix $\mathbf{R}_k = E(v_k v_k^T)$.

In the HPS-1, the $\mathbf{H}_k$ is the Jacobian matrix as follows:

$$\mathbf{H}_k = \begin{bmatrix} \mathbf{J}_F & 0_{M \times 3} & 0_{M \times 3} & 0_{M \times 3} & 0_{M \times 3} \end{bmatrix} \quad (16)$$

where

$$\mathbf{J}_F = \frac{\mathbf{P}_{\text{imu}}^n - \rho_m^n}{\|\rho_m^n - \mathbf{P}_{\text{imu}}^n\|}, \quad m = 1, 2, \ldots, M. \quad (17)$$

In the HPS-2, -3, and -4, the $\mathbf{H}_k$ is the identity matrix *diag* $(1, 1, 1, 1)$, the $\delta X$ in (13) represents the optimal state estimate after filtering, which will feed back the estimated range between the UWB anchors and relative positioning sensors in the HPS-2, -3, and -4, i.e., CAMERA, LiDAR, and RADAR, respectively. The corrected range estimation is used to solve the final position of the HPS-2, -3, and -4 by the least square.

In the HPS-6, the measurement model is written as follows:

$$Z_k = \begin{cases} \|\rho_m^n - \boldsymbol{P}_{\text{imu}}^n\| - \boldsymbol{d}_m, & m = 1, 2, \ldots, M \\ \boldsymbol{P}_{\text{camera},k}^n - \boldsymbol{P}_{\text{imu},k}^n \\ \boldsymbol{P}_{\text{lidar},k}^n - \boldsymbol{P}_{\text{imu},k}^n. \end{cases} \quad (18)$$

By linearizing (18), the measurement equation can be written as follows:

$$Z_k = \mathbf{H}_k \delta X_k + v_k$$

where $\mathbf{H}_k$ is the Jacobian matrix as follows:

$$\mathbf{H}_k = \begin{bmatrix} \mathbf{J}_F & 0_{M \times 3} & 0_{M \times 3} & 0_{M \times 3} & 0_{M \times 3} \\ \mathbf{I} & 0 & 0 & 0 & 0 \\ \mathbf{I} & 0 & 0 & 0 & 0 \end{bmatrix} \quad (19)$$

where $\mathbf{J}_F$ is the same as (17), the $\mathbf{I}$ and $\mathbf{0}$ represent the $3 \times 3$ identity and zero matrices, respectively.

The LC is realized based on the EKF in the HPS-1 and -5. The LC measurement model of the HPS-1 is expressed as follows:

$$Z_k = \boldsymbol{P}_{uwb,k}^n - \boldsymbol{P}_{imu,k}^n \quad (20)$$

where $\boldsymbol{P}_{uwb,k}^n$ is the UWB tag position calculated by the absolute positioning subsystem in the $n$ frame at $k$ time, $\boldsymbol{P}_{imu,k}^n$ is the IMU position calculated by the relative positioning subsystem in $n$ frame at $k$ time. Further, the relationship between system measurement and state is as follows:

$$Z_k = \mathbf{H}_k \delta X_k + v_k. \quad (21)$$

In this case, $\mathbf{H}_k = [\mathbf{I}\ \mathbf{0}\ \mathbf{0}\ \mathbf{0}\ \mathbf{0}]$.

In the HPS-5, the loosely coupled measurement model is written as follows:

$$Z_k = \begin{cases} \boldsymbol{P}_{\text{camera},k}^n - \boldsymbol{P}_{\text{imu},k}^n \\ \boldsymbol{P}_{\text{lidar},k}^n - \boldsymbol{P}_{\text{imu},k}^n. \end{cases} \quad (22)$$

In this case

$$\mathbf{H}_k = \begin{bmatrix} \mathbf{I} & 0 & 0 & 0 & 0 \\ \mathbf{I} & 0 & 0 & 0 & 0 \end{bmatrix} \quad (23)$$

where $\mathbf{I}$ and $\mathbf{0}$ represent the $3 \times 3$ identity matrix and $3 \times 3$ zero matrices, respectively.

*2) TC and LC-Based UKF:* The UKF is a nonlinear filtering algorithm based on the UT. It overcomes the limitations of the EKF algorithm that only uses the first-order approximation in the Taylor expansion by generating a series of particles to simulate the posterior probability density functions of the system state and measure models.

In this study, the system error state vector of HPS-1 using the UKF-TC and UKF-LC is the same as that in the EKF algorithm as shown in (8), the measurement model for the UKF-TC and -LC are in (14) and (20), respectively.

In UKF, the prestate distribution of the system is to generate a series of Sigma points by UT. Consider an $n$-dimensional random variable $\mathbf{X}$ with a mean of $\hat{x}$ and covariance of $\mathbf{P}$, transformed by a nonlinear function $f(\bullet)$. The UT generates a Sigma Vector $\mathbf{X}$ with a dimension of $2n+1$ and a set of weights $\mathbf{W}$, as follows:

$$\begin{cases} X(0) = \hat{x} \\ X(i) = \hat{x} + \left(\sqrt{(n + \lambda)\mathbf{P}}\right)_i^T & (i = 1, 2, \ldots, n) \\ X(i + n) = \hat{x} - \left(\sqrt{(n + \lambda)\mathbf{P}}\right)_i^T & (i = 1, 2, \ldots, n) \end{cases} \quad (24)$$

$$\begin{cases} W_0^{(m)} = \frac{\lambda}{n + \lambda} \\ W_0^{(c)} = W_0^{(m)} + \left(1 - \alpha^2 + \beta\right) \\ W_i^{(m)} = W_i^{(c)} = \frac{1}{2(n + \lambda)} & (i = 1, 2, \ldots, 2n) \end{cases} \quad (25)$$

$$\lambda = \alpha^2(n + \kappa) - n \quad (26)$$

where $\lambda$ is a scaling parameter to reduce the total prediction error, $\alpha$ determines the propagation speed of the Sigma sampling point around $\hat{x}$ and is usually set to a small positive number (1E-4 $\leq \alpha \leq 1$), $\kappa$ usually takes 0 in the calculation, $(\sqrt{(n + \lambda)}\mathbf{P})_i$ represents column $i$ of the square root matrix, and the candidate parameter $\beta$ is a nonnegative weight coefficient that is usually 2. $W_i^{(m)}$ and $W_i^{(c)}$ represent the weight of the mean and covariance of the $i$th sigma sample point, respectively.

The UKF algorithm processing includes the predicted update and the measurement update in two parts like the EKF, the detailed process in Appendix C.

*E. Anchor Self-Positioning*

The positions of all UWB anchors and the state of the UWB tag are simultaneously estimated by EKF-TC during the positioning process. The multilateration method was used to get the optimal initial position values for anchors.

*1) Optimal Initialization for Anchor Position:* The UWB tag is rigidly connected to the IMU with known relative positions and had a known static position measured in the field before the platform starts to move in the environment. Since the IMU provides an accurate position in a short time and is then combined with the UWB PRs, the initial values of anchor positions can be calculated by the multilateration method.

The initialization $\rho_{m,0}$ for anchor position can be obtained by minimizing the cost function

$$\rho_{m,0} = \frac{\arg\min}{\rho_m \in \mathbb{R}^3} \sum_{m=1}^{M} \left\| d_k^m - h(\rho_m^n, \rho_k^n) \right\|$$
$$h(\rho_m^n, \rho_k^n) = \left\| \rho_m^n - \rho_k^n \right\| \qquad (27)$$

where $M$ is the number of available anchors, $d_k^m$ represents the PR calculated by (6), $\rho_m^n$ are the 3-D coordinates of the $m$th anchor in the frame $n$, and $\rho_k^n$ is the 3-D coordinates of the IMU in frame $n$ at the $k$ moment. A reliable initialization result can be obtained when the number of the available anchors $M \geq 3$.

To get a reliable optimal initialization $\rho_{m,0}$, we take the mean of the initial values of anchor positions calculated by (27) within the first 30 epochs as the final $\rho_{m,0}$.

*2) Anchor Self-Positioning Based on EKF-TC:* The system state estimate $S$ has an error vector $\delta S$

$$\delta S = [\delta X \ \delta Y]^T \qquad (28)$$

where $\delta X$ is the same as (8), $\delta Y$ is the estimation error of the anchors. In this case, the measurement model is still (14). The fusion algorithm is based on EKF-TC, which estimates the system error vector $\delta S$ in real time. In our research, the $M$ was four, so the state transition matrix $\mathbf{F}_k$ and the noise-driving matrix $\mathbf{G}_k$ in (11) and (12) can be revised as follows:

$$\mathbf{F}_k = \begin{bmatrix} \mathbf{I} & dt\mathbf{I} & \mathbf{0} & \mathbf{0} & \mathbf{0} & \mathbf{0} & \mathbf{0} & \mathbf{0} & \mathbf{0} \\ \mathbf{0} & \mathbf{I} & dt\left[\mathbf{C}_{b,k}^n \mathbf{f}_k^b\right]^\times & dt\mathbf{C}_{b,k}^n & \mathbf{0} & \mathbf{0} & \mathbf{0} & \mathbf{0} & \mathbf{0} \\ \mathbf{0} & \mathbf{0} & \mathbf{I} & \mathbf{0} & -dt\mathbf{C}_{b,k}^n & \mathbf{0} & \mathbf{0} & \mathbf{0} & \mathbf{0} \\ \mathbf{0} & \mathbf{0} & \mathbf{0} & \mathbf{I} & \mathbf{0} & \mathbf{0} & \mathbf{0} & \mathbf{0} & \mathbf{0} \\ \mathbf{0} & \mathbf{0} & \mathbf{0} & \mathbf{0} & \mathbf{I} & \mathbf{0} & \mathbf{0} & \mathbf{0} & \mathbf{0} \\ \mathbf{0} & \mathbf{0} & \mathbf{0} & \mathbf{0} & \mathbf{0} & \mathbf{I} & \mathbf{0} & \mathbf{0} & \mathbf{0} \\ \mathbf{0} & \mathbf{0} & \mathbf{0} & \mathbf{0} & \mathbf{0} & \mathbf{0} & \mathbf{I} & \mathbf{0} & \mathbf{0} \\ \mathbf{0} & \mathbf{0} & \mathbf{0} & \mathbf{0} & \mathbf{0} & \mathbf{0} & \mathbf{0} & \mathbf{I} & \mathbf{0} \\ \mathbf{0} & \mathbf{0} & \mathbf{0} & \mathbf{0} & \mathbf{0} & \mathbf{0} & \mathbf{0} & \mathbf{0} & \mathbf{I} \end{bmatrix} \qquad (29)$$

$$\mathbf{G}_k = \begin{bmatrix} \mathbf{0} & \mathbf{0} & \mathbf{0} & \mathbf{0} \\ dt\mathbf{C}_{b,k}^n & \mathbf{0} & \mathbf{0} & \mathbf{0} \\ \mathbf{0} & -dt\mathbf{C}_{b,k}^n & \mathbf{0} & \mathbf{0} \\ \mathbf{0} & \mathbf{0} & dt\mathbf{I} & \mathbf{0} \\ \mathbf{0} & \mathbf{0} & \mathbf{0} & dt\mathbf{I} \\ \mathbf{0} & \mathbf{0} & \mathbf{0} & \mathbf{0} \\ \mathbf{0} & \mathbf{0} & \mathbf{0} & \mathbf{0} \\ \mathbf{0} & \mathbf{0} & \mathbf{0} & \mathbf{0} \\ \mathbf{0} & \mathbf{0} & \mathbf{0} & \mathbf{0} \end{bmatrix}. \qquad (30)$$

The Jacobian matrix $\mathbf{H}_k$ in (17) was rewritten as follows:

$$\mathbf{H}_k = \frac{\partial h}{\partial \delta S}|s = \left[\mathbf{J}_F \ \mathbf{0}_{M \times 12} \ \mathbf{0}_{M \times 3(m-1)} \ \mathbf{J}_m \ \mathbf{0}_{M \times 3(M-m)}\right] \quad (31)$$

where

$$\mathbf{J}_m = \frac{\rho_m^n - P_{\text{imu}}^n}{\left\| \rho_m^n - P_{\text{imu}}^n \right\|}, \ m = 1, \ 2, \dots, M. \qquad (32)$$

Finally, by adding the estimated error-state $\delta S$ into the predict phase of EKF, the state estimate $S$ is updated in real time.

### F. Integrity Monitoring Algorithm

This section introduces a new IM algorithm for mitigating the negative impact of NLOS. UWB PR outliers caused by NLOS from radio propagation were first removed using the received signal strength and PR differences between consequent epochs. The second phase, the so-called IBIM, used the Kalman filter innovation sequence to construct test statistics monitoring the positioning quality. Note that the EKF-LC and UKF-LC only performed the IBIM since the UWB cannot accomplish positioning alone when the number of UWB PRs was less than three.

*1) UWB Pseudo Ranges Outlier Detection:* An NLOS between the anchor and tag happens when the UWB signal is obstructed by an object, which increases the signal propagation time. Since the PR was calculated based on TOF in this study, a severe NLOS can cause a mutation in the PR, leading to a large PR difference between two adjacent epochs. Thus, an empirical power metric [45] was used as an indicator to monitor the ranging-measurement quality, defined by the difference $P_{\text{diff}}$ between the total RSS $P_{\text{RX}}$ and the RSS $P_{\text{FP}}$ of the First path (FP) component in the UWB transmission

$$P_{\text{diff}} = P_{\text{RX}} - P_{\text{FP}} = 10 * \left(C * 2^{17}/F_1^2 + F_2^2 + F_3^2\right) \quad (33)$$

where $C$, $F_1$, $F_2$, and $F_3$ are the CIR power and the amplitude of 3 points in FP, respectively.

A large $P_{\text{diff}}$ indicates possible NLOS. An empirical threshold $T_c$ was set as 0.300 m in this article to identify NLOS. In addition, $P_{\text{diff}}$ and $T_c$ were combined to identify NLOS. If the channel was subject to an NLOS situation, the corresponding PR will be eliminated, that is

$$\begin{cases} H_0: \text{LOS}, |d_m(k) - d_m(k-1)| \leq T_c \ ||P_{\text{diff}} \leq 6 \text{ dBm} \\ H_1: NLOS, |d_m(k) - d_m(k-1)| > T_c ||P_{\text{diff}} > 10 \text{ dBm} \end{cases} \quad (34)$$

where $|\bullet|$ is the absolute value at $k$ moment.

*2) Innovation-Based Integrity Monitoring:* The Kalman innovation is the difference between measurement and prediction. Both EKF and UKF follow the assumption that the process and measurement noise is the zero-mean Gaussian distribution. Based on this assumption, the Kalman innovation sequence also obeys the zero-mean Gaussian distribution, when there are no outliers in the measurement, i.e.,

$$r_k \sim N(0, \mathbf{C}_k) \qquad (35)$$

where $\mathbf{C}_k$ is the covariance matrix of the innovation $r_k$ at $k$ moment.

Therefore, the test statistic $\lambda_k$ based on the $r_k$ can be constructed as follows:

$$\lambda_k = r_k^T \mathbf{C}_k^{-1} r_k \qquad (36)$$

the $\lambda_k$ obeys the center chi-square distribution If there are no outliers in measurement, otherwise, the $\lambda_k$ will obey the noncenter chi-square distribution. Thus, according to the hypothesis test, once the value of $\lambda_k$ great than the threshold $T_d$ calculated by the Neyman–Pearson criterion [19], [91] in (37), the measurement noise matrix $\mathbf{R}$ will be rewritten as (38) to reduce the adverse effect from the outliers

$$P_{fa} = \int_{T_d}^{+\infty} \chi^2(m)dx \qquad (37)$$

where $P_{\mathrm{fa}}$ is the false alarm rate of the system, $m$ is the degree of freedom, and $m$ is the dimension of the current moment measurement vector.

Multipath propagation and the NLOS interfere with positioning leading to outliers during the Kalman filter measurement and updating process. A robust estimation performed not only will improve the positioning accuracy but also can prevent filter divergence. Some robust estimators are performed to obtain reliable parameter estimation in [92], [93], and [94]. In this article, we use a robust estimation of the measurement noise matrix $\mathbf{R}_k$ in the EKF and UKF, a revised covariance matrix of $\mathbf{R}_k$ is defined as $\widetilde{\mathbf{R}}_k$

$$\widetilde{\mathbf{R}}_k = \beta_k^{-1}\mathbf{R}_k \qquad (38)$$

where $\boldsymbol{\beta} = \mathrm{diag}[\beta_1, \beta_2, \ldots, \beta_m]$ is an equal-weight matrix of the measurements. It can be obtained empirically using the Huber weight function or IGG functions. The IGG III weight function [51] was selected here. The equivalent weight is calculated as follows [95], [96]:

$$\beta_i = \begin{cases} 1, & |s_i| \le k_0 \\ \frac{k_0}{|s_i|} \times \left\{ \frac{k_1-|s_i|}{k_1-k_0} \right\}^2, & k_0 < |s_i| \le k_1 \\ 10^{-30}, & |s_i| > k_1 \end{cases} \qquad (39)$$

where $k_0$ and $k_1$ are constants, where $k_0 = 2.5$ and $k_1 = 3.5$ in this test. $s_i$ is the normalized residual of the $i$th observation [96].

The EKF and UKF are continuously executed to obtain more robust position results after the $\widetilde{\mathbf{R}}_k$ is calculated using (39) in the measurement update phase.

## V. RESULTS, ANALYSES, AND DISCUSSIONS

The six proposed HPSs were tested in four indoor and outdoor experimental scenes to benchmark the absolute and relative positioning in both single and repeated trajectories. The experiments also evaluated the performance of the fusion methods with different sensor combinations, and the proposed IM and anchors self-positioning algorithms.

Sections V-A and V-B present the experimental results and the analyses of the results of multisensors fusion in indoor and outdoor scenes; Section V-C elaborates on the experimental results and analyses of the proposed IM algorithm; the results of the proposed anchors self-positioning algorithms are presented and analyzed in details in Section V-D. All six HPSs in this benchmark leveraged the proposed IM algorithm.

### A. Results of the Indoor Scenarios

Extensive experiments were carried out to validate the six HPSs in two indoor experimental scenarios. The positioning methods of the UWB, the CAMERA+IMU, and the LIDAR were the multilateration, the ORB-SLAM3, and the A-LOAM, respectively. The mmWave RADAR was conducted only in underground parking (Indoor-II) scenes because of the sensor availability.

*1) Indoor-I Experimental Results and Analyses:* The trajectories of the proposed HPSs in Indoor I case are presented in Fig. 8. Fig. 8(a) and (c) presented the single and repeated trajectories of the HPS-1 (UWB+IMU) and HPS-6 (UWB+IMU+CAMERA+LIDAR), respectively. Fig. 8(b) and (d) showed the single and repeated trajectories of the trajectories of HPS-2 (UWB+CAMERA+IMU), HPS-3 (UWB+LIDAR), and HPS-5 (IMU+CAMERA+LIDAR), respectively. For comparison, the high-quality millimeter-level ground truth and UWB trajectories are also plotted in all subfigures. The positioning trajectories from CAMERA+IMU and LIDAR were also presented in Fig. 8(b) and (d).

As shown in Fig. 8, the UWB positioning displayed mutations in local areas due to NLOS impacts. The CAMERA+IMU positioning accumulated clear deviations from the ground truth over time, though the stereo-inertial mode was used which was supposed to be more robust than the single-camera or stereo camera without IMU. LIDAR trajectories showed similar deviations but were clearly less significant.

These results indicated that the passive camera system accumulated larger positioning errors than the active LIDAR system in the experiment scenario. Meanwhile, it was worth noting that the performance of the LIDAR hardware itself was superior to the camera system used in the experiment. The fused trajectories of the HPSs were all closer to the ground truth and smoother than the absolute UWB trajectory alone. The HPS-2 (UWB+CAMERA+IMU) trajectory was still close to the ground truth, which showed that the fusion of relative and absolute positioning improves trajectory accuracy.

The cumulative distribution function (CDFs) of error corresponding to the trajectories in Fig. 8 are shown in Fig. 9. As the path length increased, the positioning accuracy of CAMERA+IMU drifted significantly, where the positioning accuracy was the lowest among all positioning methods and the differences were sharp. LIDAR positioning also drifted but was not significant in a short time span, e.g., in a single trajectory.

According to Fig. 9, the positioning accuracies of HPSs were all higher than that of the single positioning solution. As far as HPS-1 was concerned, the positioning accuracy of the four fusion methods was equivalent, and the positioning accuracy of the UKF-TC was slightly higher than the other three. Since HPS-1's state and observation model were both nonlinear, the UKF has a higher positioning accuracy than the EKF. The improvements were significant by using HPS-2 (UWB+CAMERA+IMU) and HPS-3 (UWB+LIDAR) fusion, where the HPS-3 had the highest positioning accuracy.
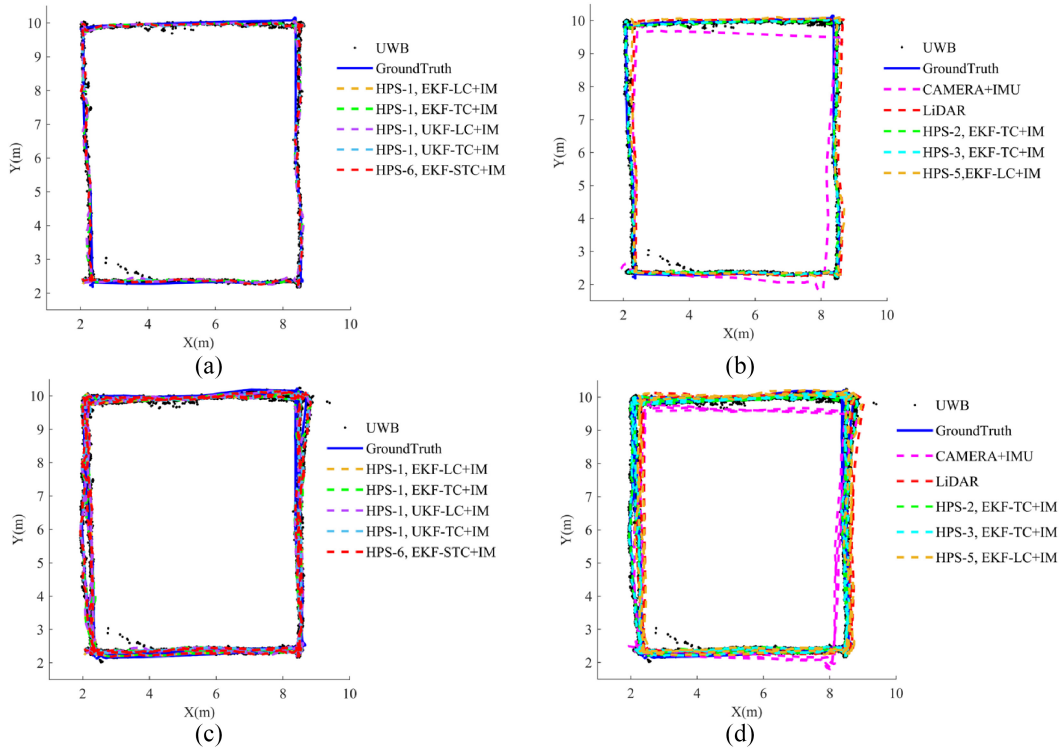
Fig. 8.   Trajectories in Indoor I (a) and (c) trajectories of the HPS-1 and HPS-6 of Indoors I-1 and I-3, respectively; (b) and (d) related trajectories of the CAMERA, LiDAR, and UWB for Indoors I-1 and I-3, respectively.

HPS-5 (IMU+CAMERA+LIDAR) that fused three relative positioning techniques achieved more accurate positioning results than the absolute positioning (UWB) alone in Indoor-I environment. This result raised an interesting question on whether a combined relative positioning can substitute absolute positioning alone. A more general conclusion required more experiments in different scenarios.

HPS-6 (UWB+IMU+CAMERA+LIDAR) combined all active/passive solutions, but the results were not the best. This result indicated that there is an accuracy limit for the hybrid positioning. The improvement of the overall fusion accuracy will reduce, especially when the accuracy of particular or multiple sensors was low.

Three error statistical indicators, i.e., maximum, mean, and root mean square (RMS) errors, were used to evaluate the positioning accuracy. The error statistics corresponding to the trajectories in Fig. 8 are shown in Fig. 10.

The proposed hybrid positioning solutions improved the ARP alone, according to the maximum, mean, and RMS errors in Fig. 10. In Indoor I-1, the maximum errors of the UWB, CAMERA+IMU, and LIDAR were 0.574, 0.857, and 0.409 m, respectively; and the maximum error of the HPS-1 (UWB+IMU, UKF-TC+IM), HPS-2 (UWB+CAMERA+IMU), and HPS-3 (UWB+LIDAR) were 0.354, 0.531, and 0.323 m, respectively, which reduced by 38.33%, 38.04%, and 21.03% errors after fusing the relative positioning and absolute positioning in comparison with UWB, CAMERA+IMU, and LIDAR. The RMS errors of four fusion algorithms in the HPS-1 (UWB+IMU) were nearly the same (around 0.210 m).

The HPS-3 (UWB+LIDAR) has the highest average positioning accuracy in Indoor I. The maximum, mean, and RMS errors of the LIDAR were 0.470, 0.261, and 0.235 m in Indoor I-3, respectively; and the corresponding errors of the HPS-3 were 0.396, 0.164, and 0.178 m in this case, respectively, where UWB-LIDAR fusion reduced LIDAR positioning errors by 15.74%, 37.16%, and 24.26%, respectively.

The RMS error of the HPS-5 (IMU+CAMERA+LIDAR), i.e., 0.206 m in Indoor I-1 and 0.222 m in Indoor I-3. The higher accuracy of HPS-5 than the UWB, CAMERA+IMU, and LIDAR, as shown in Fig. 10, was because the LIDAR has reliable performance and the fusion of IMU and LIDAR further improves the accuracy than the LIDAR alone. The maximum, mean, and RMS errors of the HPS-6 (UWB+IMU+CAMERA+LIDAR) were 0.523, 0.201, and 0.212 m in Indoor I-3, respectively, approximately the same as that of the HPS-1 (UWB+IMU, EKF-TC+IM), which indicated that in the indoor environment, CAMERA, and LIDAR improve little in addition to the UWB+IMU.

*2) Indoor-II Experimental Results and Analyses:* The trajectories of the six HPSs in Indoor-II case are illustrated in Fig. 11. Fig. 11(a) and (c) presented the single and repeated trajectories of the HPS-1 (UWB+IMU) and HPS-6 (UWB+IMU+CAMERA+LIDAR), respectively, Fig. 11(b) and (d) showed the single and repeated trajectories of the trajectories of HPS-2 (UWB+CAMERA+IMU), HPS-3 (UWB+LIDAR), HPS-4 (UWB+RADAR), and HPS-5 (IMU+CAMERA+LIDAR), respectively.

For comparison, the ground truth and UWB trajectories are also plotted in all subfigures. The positioning trajectories from
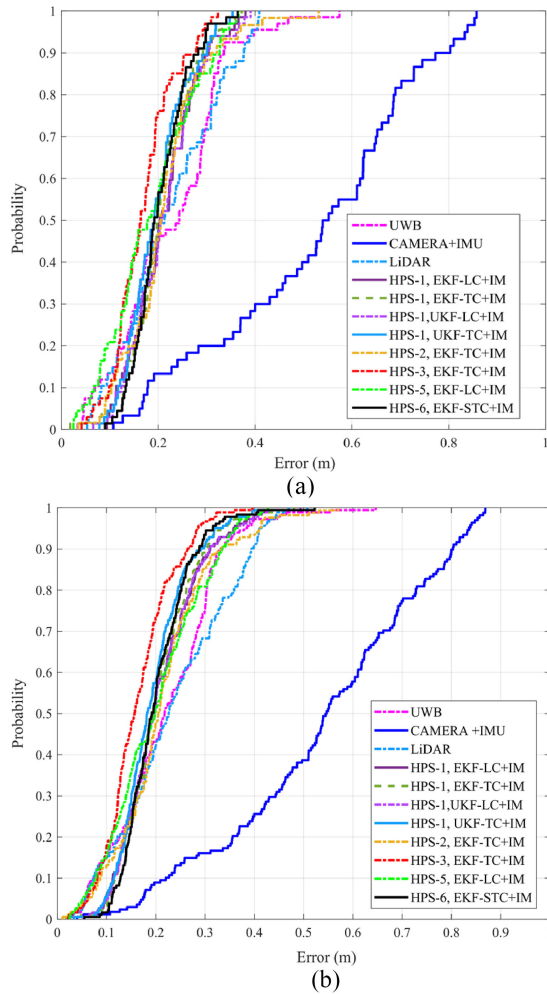
(a)



(b)

Fig. 9. CDFs of different positioning methods in the (a) Indoor I-1 and (b) Indoor I-3.



The positioning error of the Indoor I-1

(a)



The positioning error of the Indoor I-3

(b)

Fig. 10. Statistics of different positioning methods in the (a) Indoor I-1 and (b) Indoor I-3.

CAMERA+IMU, RADAR, and LIDAR were also presented in Fig. 11(b) and (d) for comparison.

Indoor II has a rectangular area without signal obstructions, such as tables and chairs. According to Fig. 11, the trajectories of the proposed six HPSs are closer to the ground truth compared to the trajectories of the UWB, CAMERA, LIDAR, and RADAR alone. Again, the trajectories of the CAMERA, RADAR, and LIDAR drifted over time, but the positioning accuracies after the UWB fusion were significantly improved.

The CDFs and error statistics corresponding to the trajectories in Fig. 11 are shown in Figs. 12 and 13, respectively.

As shown in Fig. 12, the six HPSs have higher positioning accuracy than that of the absolute positioning subsystem using UWB and the relative positioning subsystem using CAMERA+IMU, LIDAR, and RADAR.

According to Fig. 12(a) and (c), the positioning accuracy of HPS-1 (UWB+IMU, EKF-TC+IM) and HPS-6 (UWB+IMU+CAMERA+LIDAR) were almost the same, similar to the results in Indoor I. The maximum positioning error of HPS-1 and HPS-6 was less than 0.250 m, much smaller than HPS-2 (UWB+IMU+ CAMERA) and HPS-4 (UWB+RADAR), i.e., 1.100 and 1.650 m, respectively. The mean error of the four fusion methods of the HPS-1 was less
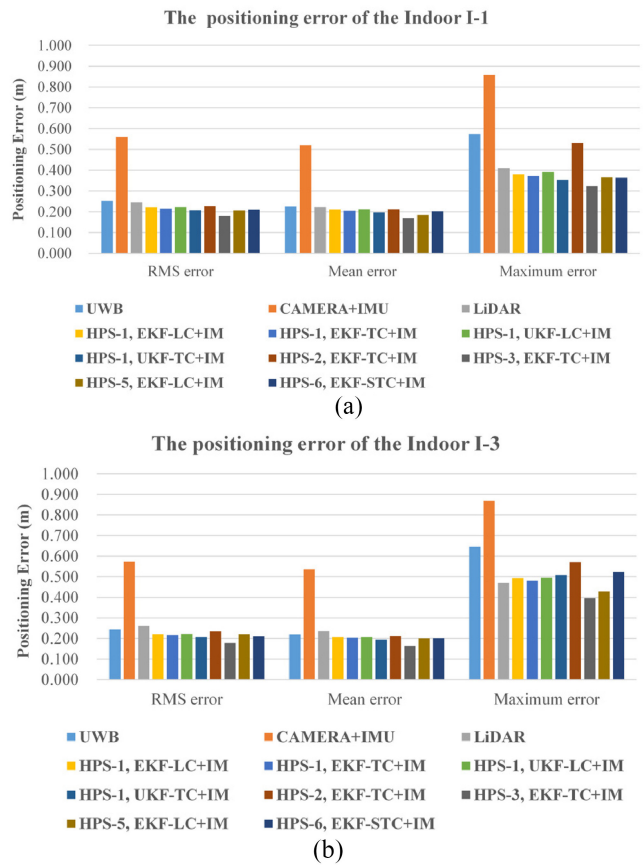
than 0.080 m. For the UWB-IMU fusion, the results show that the positioning accuracy of TC was slightly higher than that of LC, and the accuracy of UKF fusion was slightly higher than that of EKF.

According to Fig. 12(b) and (d), the maximum positioning error of the CAMERA+IMU was around 1.100 m, and the maximum positioning error of the HPS-2 (UWB+ CAMERA+IMU) was no more than 0.450 m, which indicates that the absolute positioning can significantly improve the positioning accuracy.

Among three relative positioning techniques, i.e., CAMERA, RADAR, and LiDAR, LiDAR has the highest positioning accuracy. The maximum LiDAR positioning error was less than 0.200 m in Indoor II-1. The maximum positioning error of the HPS-5 (IMU+CAMERA+LiDAR) was no more than 0.300 m in Indoor II-1, which clearly reduced the errors in IMU+CAMERA, i.e., more than 1.000 m.

The maximum positioning errors of the RADAR were 1.228 and 1.683 m in Indoors II-1 and II-3, respectively. Nevertheless, the HPS-4 (UWB+RADAR) effectively suppressed the RADAR drift. As the path length increased, the positioning accuracy of RADAR drifted seriously. The RADAR positioning accuracy was the lowest among all positioning methods and the differences were sharp.

According to Fig. 13(a) and (b), the RMS, mean, and maximum errors of the six HPSs were all smaller than that of a single positioning system. In this test, the positioning error of
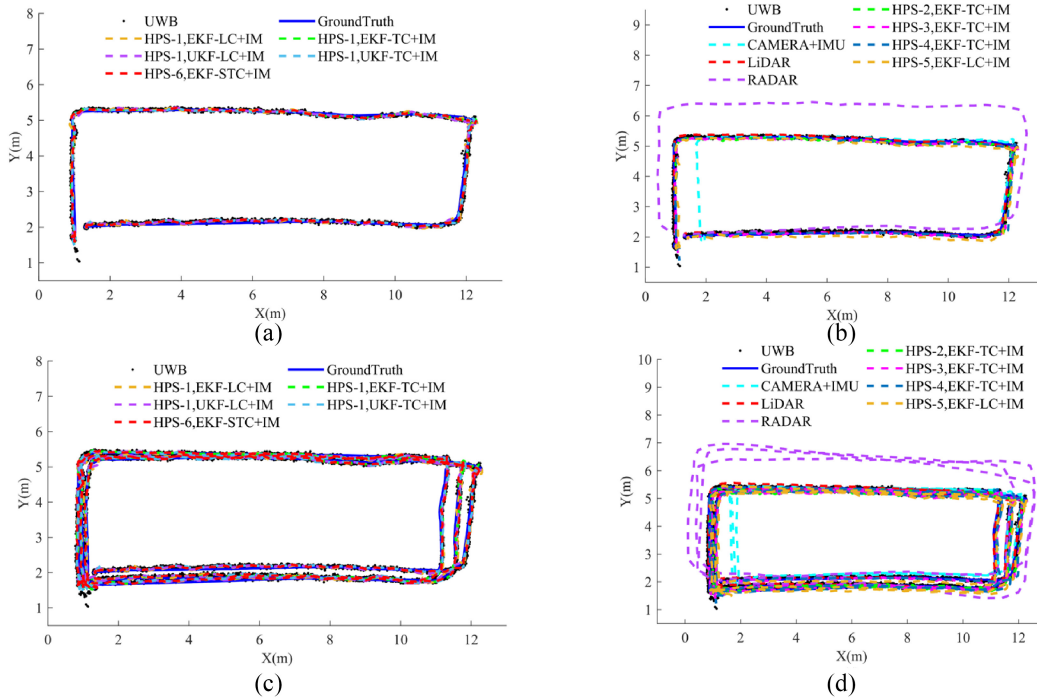
Fig. 11. Positioning trajectories in Indoor II. (a) and (c) Trajectories of the HPS-1 and HPS-6 of Indoors II -1 and -3, respectively. (b) and (d) Trajectories of HPS-2, -3, -4, -5 using the CAMERA, LiDAR, RADAR, and UWB in Indoors II-1 and -3, respectively.
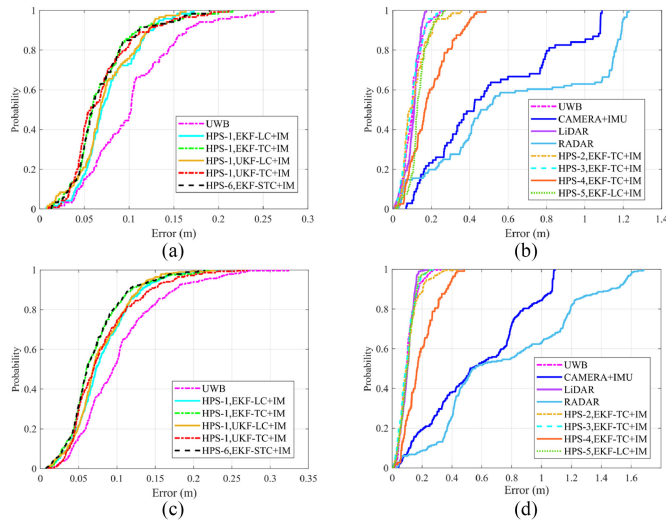


Fig. 12. CDFs of different positioning methods in the (a) and (b) Indoor II-1 and (c) and (d) Indoor II-3.



Fig. 13. Statistics of different positioning methods in the (a) Indoor II-1 and (b) Indoor II-3.

RADAR and CAMERA+IMU was relatively large, and the positioning accuracy of LiDAR was almost the same as that of UWB and the HPS-3 (UWB+LiDAR).

As far as HPS-1 (UWB+IMU) is concerned, the four fusion methods can effectively fuse the UWB and IMU. The positioning accuracy of TC was slightly higher than that of LC. No significant difference between EKF and UKF in this study. The maximum, mean, and RMS errors of the UWB were 0.324, 0.102, and 0.116 m in Indoor II-3, respectively, the maximum, mean, and RMS error of the HPS-1 (UWB+IMU, EKF-TC+IM) was 0.226, 0.071, and 0.078 m in Indoor II-3.

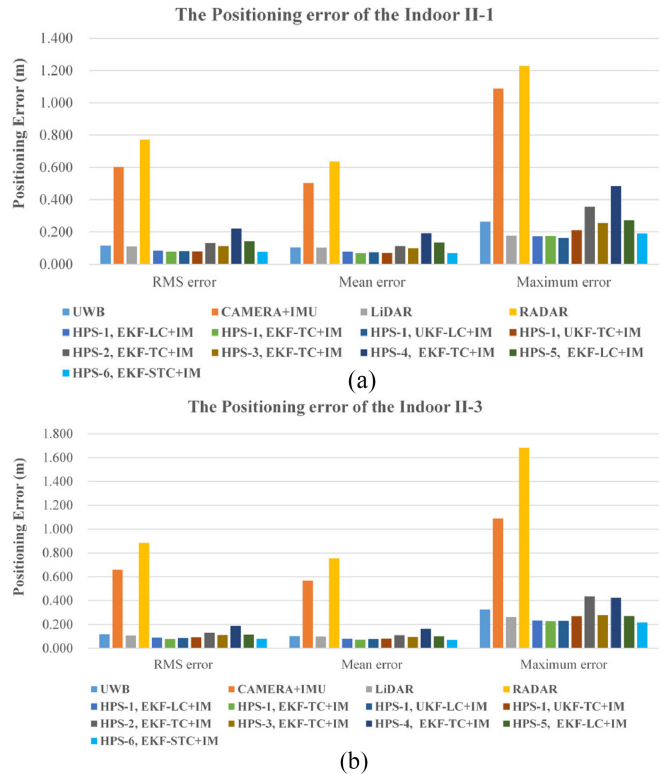The maximum, mean, and RMS errors of the CAMERA+IMU were 1.089, 0.568, and 0.659 m in

Indoor II-3, respectively, and the maximum, mean, and RMS errors of the HPS-2 (UWB+ CAMERA+IMU) was 0.434, 0.108, and 0.129 m in Indoor II-3. Fusing UWB and CAMERA+IMU reduced errors by 60.140%, 80.090%, and 80.420%, respectively.
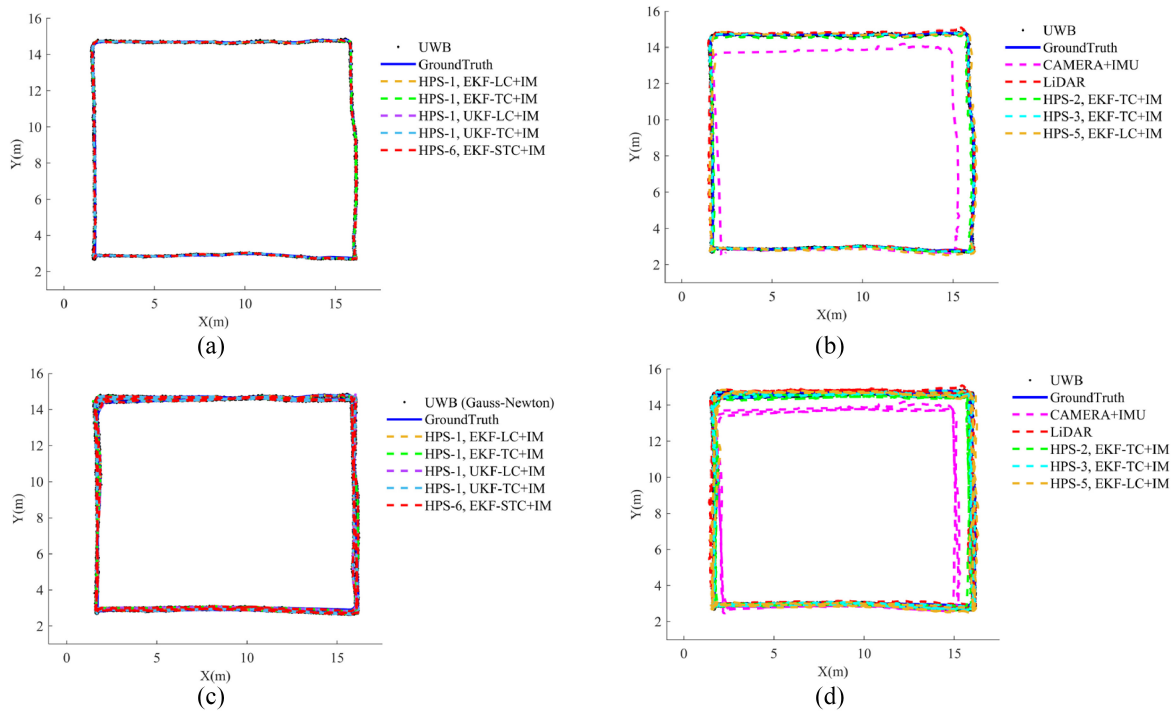
Fig. 14. Positioning trajectories in the Outdoor I. (a) and (c) Trajectories of the HPS-1 (UWB+IMU) and HPS-6 (UWB+IMU+CAMERA+LiDAR) of Outdoors I-1 and -3, respectively. (b) and (d) Related trajectories of the CAMERA, LiDAR, and UWB for the Outdoors I-1, and -3, respectively.

The maximum error of the RADAR was 1.228 m in Indoor II-1 and 1.683 m in Indoor II-3. The maximum error of the HPS-4 (UWB+RADAR) was 0.531 m in Indoor II-1, and 0.605 m in Indoor II-3. fusing UWB and RADAR reduced 16.77% and 25.680% errors. The mean and RMS errors of the RADAR in Indoor II-3 were 0.754 and 0.884 m, respectively, and were 0.163 m, and 0.189 m in the HPS-4, which were reduced by 78.380% and 78.620% after fusing the UWB and RADAR in comparison with RADAR alone, respectively.

The accuracy of the HPS-5 (IMU+CAMERA+LIDAR) was slightly higher than that of the UWB alone. Similar to the findings in Indoor-I, this result indicated that the HPS-5 may substitute the absolute UWB positioning and can be used in environments where the deployment of UWB was not practical.

The maximum, mean, and RMS errors of the HPS-6 (UWB+IMU+CAMERA+LIDAR) were 0.214, 0.070, and 0.080 m in Indoor II-3, respectively, smaller than the HPS-6 in Indoor I-3. This result indicated that the UWB had better performance in the open area, e.g., in Indoor II.

### B. Results of the Outdoor Scenarios

In this section, we presented the experimental results in an empty outdoor square and an empty basketball court. The outdoor-related experiments of the RADAR were only presented in basketball court (Outdoor-III) scenes to compare with experimental results of other positioning methods.

*1) Outdoor-I Results and Analyses:* The trajectories of Outdoor I-1 and Outdoor I-3 are plotted in Fig. 14 in a similar

pattern to the Indoor cases. Fig. 14(a) and (c) presented the single and repeated trajectories of the HPS-1 (UWB+IMU) and HPS-6 (UWB+IMU+CAMERA+LIDAR), respectively. Fig. 14(b) and (d) showed the single and repeated trajectories of the trajectories of HPS-2 (UWB + CAMERA + IMU), HPS-3 (CAMERA + LIDAR), and HPS-5 (IMU+ CAMERA + LIDAR), respectively.

For comparison, the ground truth and UWB trajectories are also plotted in all subfigures. The positioning trajectories from CAMERA+IMU and LIDAR are also presented in Fig. 14(b) and (d) for comparison.

As shown in Fig. 14, there were no abnormal values in the UWB positioning trajectory, and the positioning trajectory was close to the ground truth. The CAMERA+IMU positioning trajectory gradually deviated from the ground truth as the length of the test path increased.

The LIDAR positioning trajectory also deviated from the ground truth over time, but the deviation was much smaller than that of the CAMERA+IMU. The HPSs were all close to the ground truth.

The CDFs of positioning error and error statistical values corresponding to the trajectories in Fig. 14 are shown in Figs. 15 and 16.

As shown in Fig. 15, the HPS-1 (UWB+IMU, UKF-TC+IM, EKF-TC+IM) outperformed all other positioning methods. The mean positioning errors of HPS-1 (UWB+IMU) using UKF-TC+IM and EKF-TC+IM were both around 0.090 m. The positioning means error of the HPS-2 (UWB+CAMERA+IMU) and the HPS-3 (UWB+LIDAR) were both around 0.180 m. In this experiment, the positioning error of the CAMERA+IMU was greater than that of Indoor I scene due to the reason that Outdoor-I scene had fewer texture
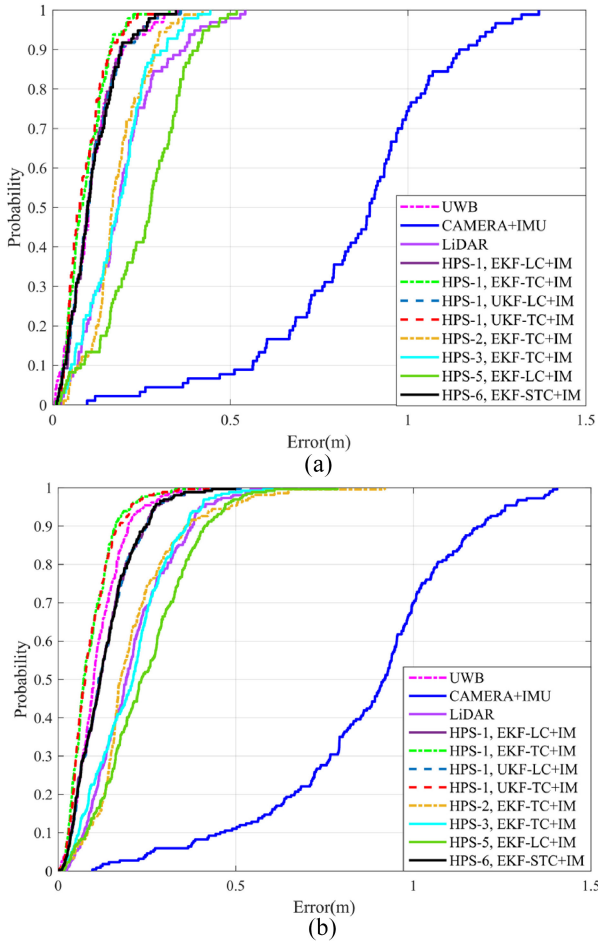
Fig. 15. CDFs of different positioning methods in the (a) Outdoor I-1 and (b) Outdoor I-3.



Fig. 16. Statistics of different positioning methods in the (a) Outdoor I-1 and (b) Outdoor I-3.

features than Indoor-I scene. However, the HPS-2 (UWB+ CAMERA+IMU) significantly improved the positioning in comparison with CAMERA+IMU, which showed that absolute positioning can significantly improve the relative position, especially when the relative positioning was unreliable. The HPS-5 (IMU+CAMERA+LIDAR) had the lowest positioning accuracy among different HPSs since the positioning accuracies of LIDAR and CAMERA was relatively low in Outdoor-I. The HPS-6 (UWB+IMU+CAMERA+LIDAR) improved the positioning accuracy in comparison with HPS-5 by adding the UWB positioning.

As shown in Fig. 16, the mean positioning error of the UWB was 0.110 m. In HPS-1 (UWB+IMU), the TC had a slightly higher positioning accuracy than the LC, and the positioning accuracy of the LC was almost the same as the UWB positioning alone. These results showed that, without NLOS, UWB was accurate and the improvement of adding IMU to UWB was minor. The maximum, mean, and RMS errors of the HPS-1 (EKF-TC+IM, UKF-TC+IM) were around 0.400, 0.090, and 0.110 m, respectively. The HPS-1 had the smallest maximum error among all HPSs in Outdoor I-1, which was less than 0.370 m.

The maximum positioning error of CAMERA+IMU was 1.400 m, larger than that in Indoor scenes, i.e., 0.900 and 1.100 m in Indoors I and II, respectively. Similar to Indoor
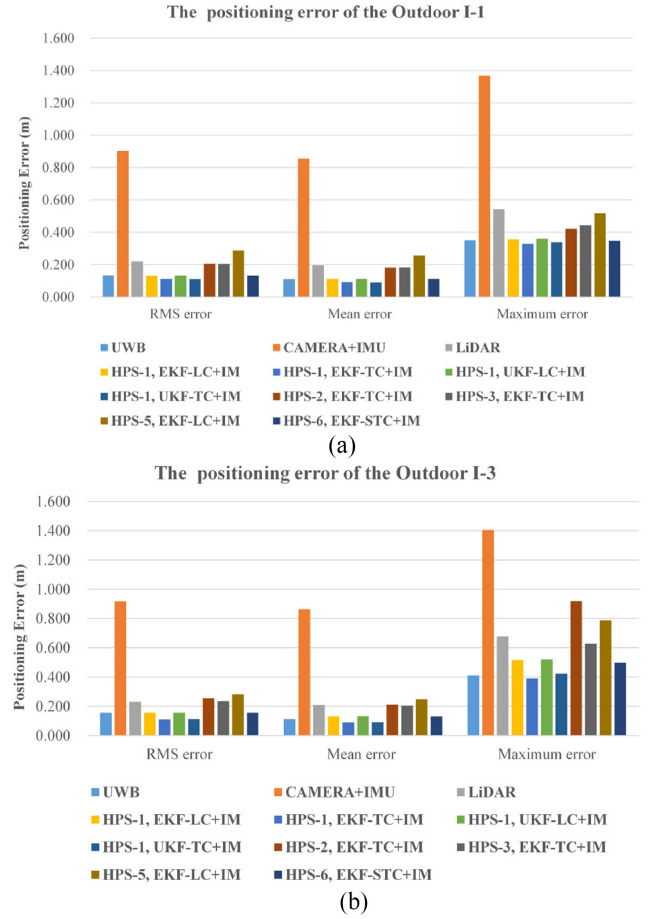
scenes, vision positioning in HPS-2 (UWB+CAMERA+IMU) had a significant improvement, i.e., the RMS errors were 0.904 and 0.918 m in the CAMERA+IMU and were 0.206 and 0.253 m in HPS-2 in Outdoors I-1 and I-3, respectively, which reduced by 77.21% and 72.44% after fusing the UWB and CAMERA+IMU, respectively.

The maximum error of LIDAR was 0.678 m in Outdoor I-3, which was larger than that of the two Indoor cases (0.470 and 0.260 m in Indoors I-3 in II-3). This was because more objects existed in indoor than outdoor scenes, which provided a more reliable matching in the indoor scenarios. The maximum, mean, and RMS errors of the LIDAR were around 0.678, 0.209, and 0.231 m for Outdoor I-3, respectively. The maximum, mean, and RMS errors of the HPS-3 (UWB+LIDAR) were around 0.629, 0.200, and 0.231 m for Outdoor I-3, respectively. The HPS-3 further improved the positioning accuracy compared to LIDAR positioning alone.

The positioning accuracy of HPS-5 (IMU+CAMERA+LIDAR) was lower than that of UWB due to the rapid drift errors over time in this case. However, by fusing relative IMU and LIDAR positioning, the HPS significantly suppressed the error drift caused by the camera.

The mean error of the HPS-6 was very similar to that of the UWB in Outdoor I-1, which indicated that UWB had reliable performance in an open area and additional vision
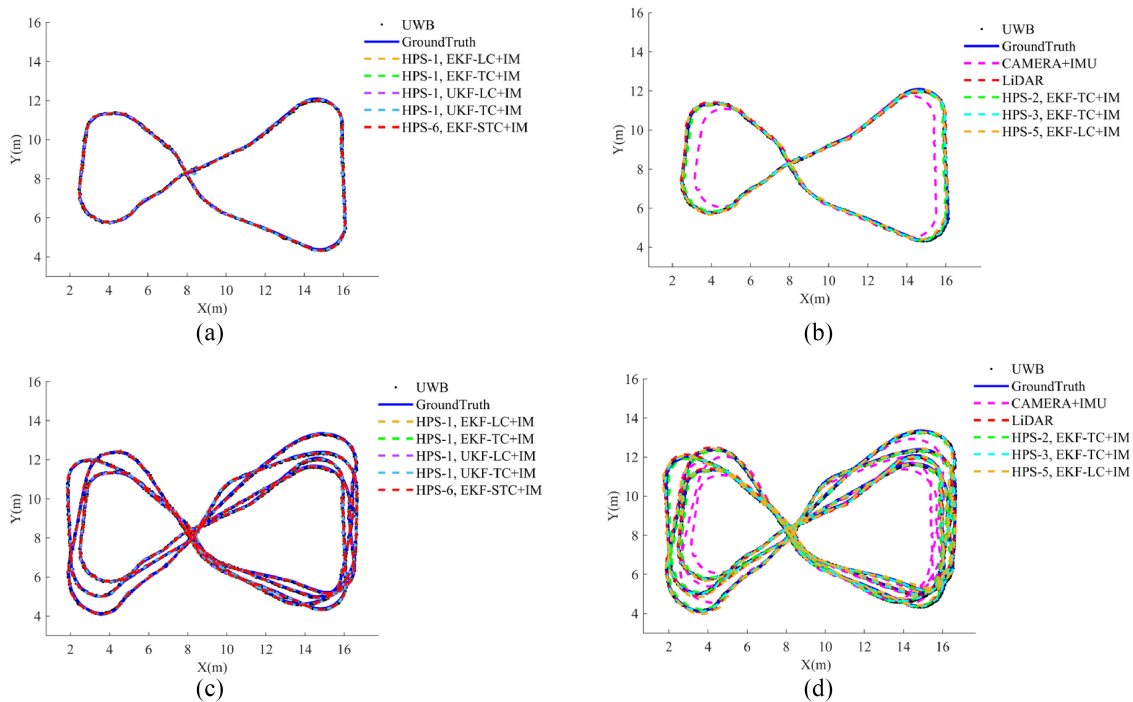
Fig. 17.   Positioning trajectories in the Outdoor II. (a) and (c) Trajectories of the HPS-1 (UWB+IMU) and HPS-5 (UWB+IMU+CAMERA+LiDAR) of Outdoors II-1 and -3, respectively. (b) and (d) Related trajectories of the CAMERA+IMU, LiDAR, and UWB for the Outdoors II-1, and -3, respectively.

and IMU did not improve the positioning accuracy anymore. As the trajectory length increased, the positioning accuracy of CAMERA+IMU and LIDAR decreased, resulting in the mean error of the HPS-6 being slightly lower than that of UWB alone in Outdoor I-3. The mean errors of the HPS-6 and UWB were 0.130 and 0.110 m, respectively.

*2) Outdoor-II Results and Analyses:* The trajectories of the eight-shape test (i.e., Outdoor II-1 and Outdoor II-3) are shown in Fig. 17 in a similar pattern as in Fig. 14.

According to Fig. 17, the trajectories of the proposed HPSs were close to the ground truth. No mutations in the UWB positioning trajectories were noticed, which indicated that the UWB signal was in an LOS environment.

The trajectories of the HPS-1 and the HPS-6 almost coincide as can be seen from Fig. 17(a) and (c), which indicated that the camera and LIDAR positioning did not improve the results of UWB+IMU. The trajectories of the CAMERA+IMU still had the largest deviation from the ground truth. The longer the trajectory length, the more significant the deviations.

Compared with Outdoor I, the trajectory of the LIDAR in Outdoor II was closer to the ground truth. One possible reason was that more laser beams were returned in this experiment than in Outdoor-I. In Outdoor II, the initial position was the middle of the square, at the intersection of the eight shaped. The reflected laser beams from the surrounding objects, e.g., trees, were more than that in Outdoor I. Since the trajectory was close to the edge of the scene in Outdoor II, most of the laser beams were reflected come from the tree trunk. Therefore, the LIDAR ranging and positioning accuracy in Outdoor II was higher than in Outdoor I.

The CDFs of positioning error and error statistical values corresponding to the trajectories in Fig. 17 are shown in Figs. 18 and 19, respectively.

According to Fig. 18, the positioning accuracies of the HPS-1, -3, -5, and -6 were nearly equal in Outdoor II, e.g., the 90% positioning error of the HPS-1, -3, -5, and -6 were within 0.020 m. The proposed HPSs all improved the positioning accuracies of the relative positioning, and the improvement in the CAMERA+IMU accuracy was particularly significant. The UWB and LiDAR have almost the same positioning accuracy in this experiment. The positioning accuracies of the HPS-3 (mean error was 0.080 m) were higher than that of the HPS-3 in Outdoor I. The positioning accuracies of the HPS-5 (mean error was 0.090 m) in Outdoor II were higher than that of HPS-5 in Outdoor I since the positioning accuracies of the LiDAR in Outdoor II were higher.

According to Fig. 19(a) and (b), the maximum and mean positioning errors of the HPS-1 (UWB+IMU) were within 0.250 m and around 0.080 m in Outdoor II-1, respectively. The positioning accuracy of the four fusion algorithms of the HPS-1 was nearly equal in Outdoors II-1 and II-3.

The maximum error of the CAMERA+IMU was 0.720 and 1.028 m in Outdoors II-1 and II-3, respectively. The maximum errors of the HPS-2 (UWB+CAMERA+IMU) were 0.290 and 0.553 m in Outdoors II-1 and II-3, respectively, which was 59.73%, and 46.28% lower than the CAMERA+IMU by adding the UWB, respectively.

The positioning accuracy of the HPS-3 (UWB+LIDAR) was slightly higher than that of the LIDAR in Outdoor II-3, i.e., maximum, mean, and RMS errors of the HPS-3 were 0.345, 0.083, and 0.127 m, respectively. The mean and RMS
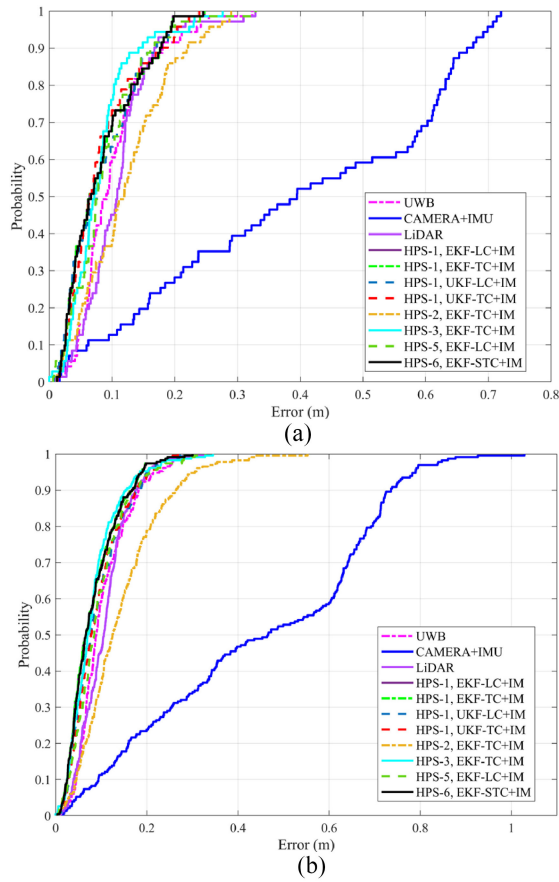
Fig. 18. CDFs of different positioning methods in the (a) Outdoor II-1 and (b) Outdoor II-3.



Fig. 19. Statistics of different positioning methods in the (a) Outdoor II-1 and (b) Outdoor II-3.

errors of the HPS-5 (i.e., 0.094 and 0.110 m) were slightly lower than that of the UWB (i.e., 0.104 and 0.119 m) in this experiment. The HPS-6 (UWB + IMU + CAMERA+LIDAR) effectively achieved absolute positioning using the UWB and relative positioning based on IMU, CAMERA, and LIDAR. The mean and RMS errors of the proposed HPSs were almost the same in this experiment, which shows that in a simple scenario (without NLOS, and abundant visual textures), the positioning accuracies of all solutions were almost equally good.

*3) Outdoor-III Results and Analyses:* The third outdoor experimental scene was an empty basketball court. In this experimental scene, CAMERA+IMU has failed due to insufficient visual texture features, thus, no CAMERA+IMU outcomes are to be reported. RADAR trajectories were presented and compared with other methods. The positioning trajectories in this scene are shown in Fig. 20 in a similar layout as in Fig. 14.

It can be seen from Fig. 20(a) and (c) that the trajectories of HPS-1 and HPS-6 did not deviate significantly from the trajectories of the ground truth. There was no abnormal jumping point in the UWB positioning result, which indicated that the UWB signal was in the LOS environment. According to Fig. 20(b) and (d), the trajectories of RADAR gradually deviated from the ground truth over time. As the length of the driving path increased, the deviation became more and more serious. The fusion of UWB and RADAR gave a trajectory
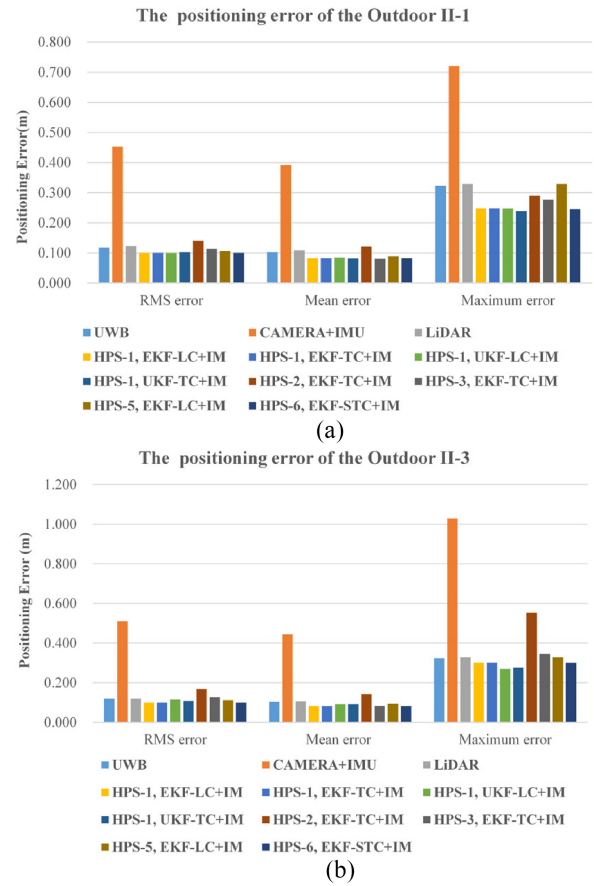
close to the ground truth. The positioning trajectories of the LIDAR did not deviate from the ground truth in this case, and the HPS-3 (UWB+LIDAR) trajectory was also close to the ground truth in Outdoors III-1 and -3. Note that the HPS-5 fused the IMU and LIDAR sensors in this test, and HPS-6 fused the UWB, IMU, and LIDAR sensors, without CAMERA in comparison with previous ones.

The CDFs of positioning error and error statistical values corresponding to the trajectories in Fig. 20 are shown in Figs. 21 and 22, respectively.

As shown in Fig. 21, as far as the HPS-1 was concerned, the positioning accuracies of the four methods were nearly equal, and the maximum error of the HPS-1 was no more than 0.400 m; the positioning accuracy of TC was slightly higher than that of LC.

The positioning accuracy of HPS-6 was almost equal to that of HPS-1 (HPS-1, EKF-TC+IM). Comparing Fig. 21(b) and (d). The RADAR positioning accuracy drifted seriously, i.e., the maximum error was around 1.683 and 4.661 m in Outdoors III-1 and III-3, respectively. Compared with Indoor II scenes, the RADAR had a lower positioning accuracy in this scene. This was because on one side of the basketball court in this test scene, there were few visual targets, e.g., buildings or objects, resulting in a decrease in positioning accuracy. Nevertheless, the fusion of the positioning accuracy was significantly improved after the fusion of UWB and RADAR.
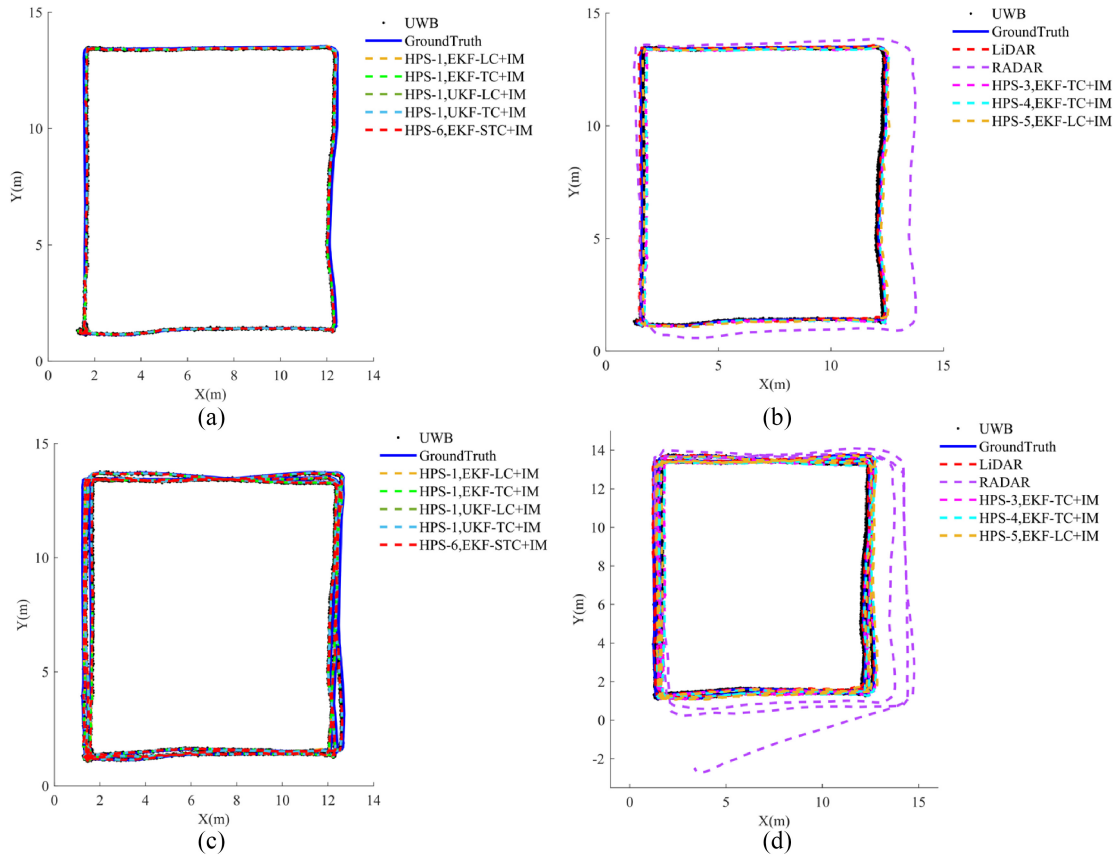
Fig. 20. Positioning trajectories in the Outdoor III. (a) and (c) Trajectories of the HPS-1 (UWB+IMU) and HPS-6 (UWB+IMU+LiDAR) of Outdoors III-1 and -3, respectively. (b) and (d) Related trajectories of the LiDAR, RADAR, and UWB for the Outdoors III-1, and -3, respectively.
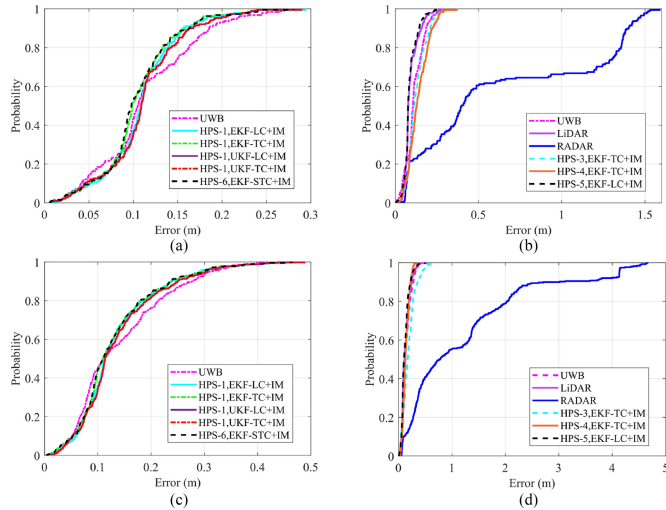


Fig. 21. CDFs of different positioning methods in the (a) Outdoor III-1 and (b) Outdoor III-3.

According to Fig. 22(a) and (b), the positioning accuracy of the HPS-1, -3, -5, and -6 was almost equivalent. The maximum, mean, and RMS errors of the HPS-1, -3, -5, and -6 were around 0.450, 0.130, and 0.150 m in Outdoor III-3, respectively. Compared with other HPSs, the positioning accuracy of HPS-4 (UWB+RADAR) was slightly lower than that of other HPSs due to the effect stemming from the poor positioning performance of the RADAR.

The maximum error of the LIDAR was 0.282 and 0.541 m in Outdoors III-1 and III-3. The maximum, mean, and RMS errors of the RADAR were 4.661, 1.215, and 1.701 m in Outdoor III-3, respectively. The maximum, mean, and RMS errors of the HPS-4 (UWB+RADAR) were 0.550, 0.150, and 0.180 m in Outdoor III-3, respectively, which reduced 89.42%, 87.65%, and 88.19% after fusing the UWB and RADAR in comparison with RADAR alone, respectively. The HPS-5 (IMU+ LIDAR) formed by the fusion of two relative positioning sensors can achieve almost the same positioning accuracy as using UWB absolute positioning in this test scenario, similarly to in Indoor-I and Indoor-II.

## C. IM Algorithm Results and Analyses

The proposed IM algorithm monitored the data quality using the UWB PR and RSS. In this section, the experimental results of the IM in indoor and outdoor scenes are presented, respectively.

*1) Indoor Scene:* In Indoor I scene, the occlusion of UWB signals by tables and chairs caused NLOS propagation. Therefore, Indoor I scene was selected to test the outlier detection performance of the proposed IM algorithm. To fully test the performance of the proposed algorithm, we chose an experiment with a ground truth length of 84.800 m, i.e., Indoor I-3, to test and analyze the IM
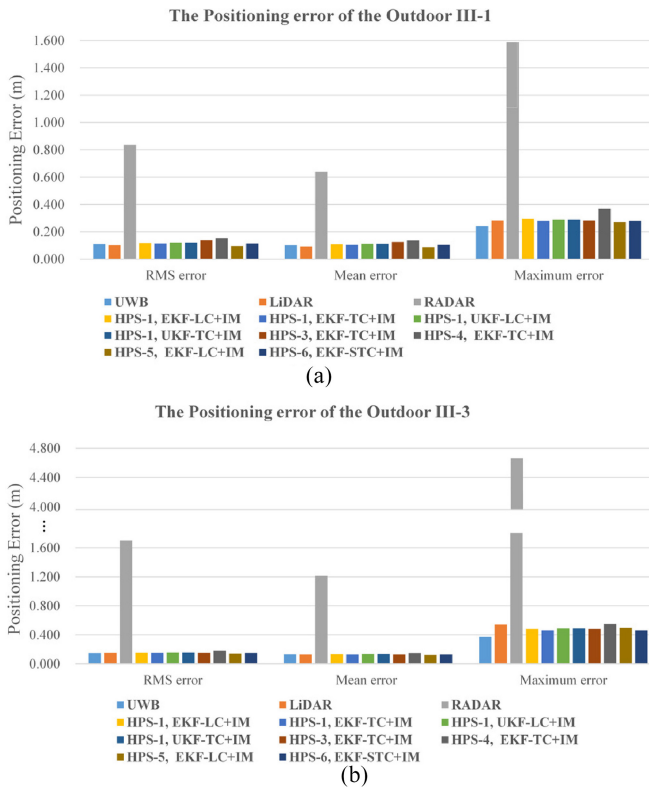
Fig. 22. Statistics of different positioning methods in the (a) Outdoor III-1 and (b) Outdoor III-3.
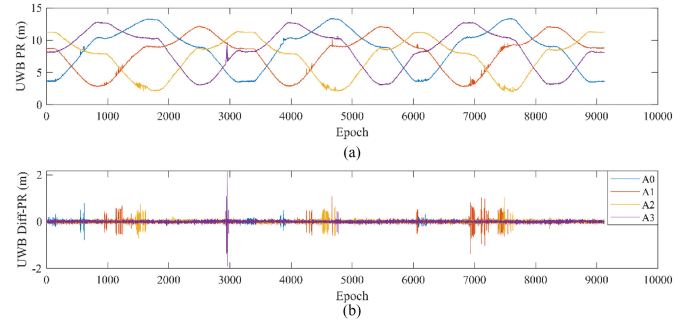


Fig. 23. UWB PRs of four Anchors in Indoor I-3. (a) UWB PRs. (b) Difference of the PR between adjacent epochs.
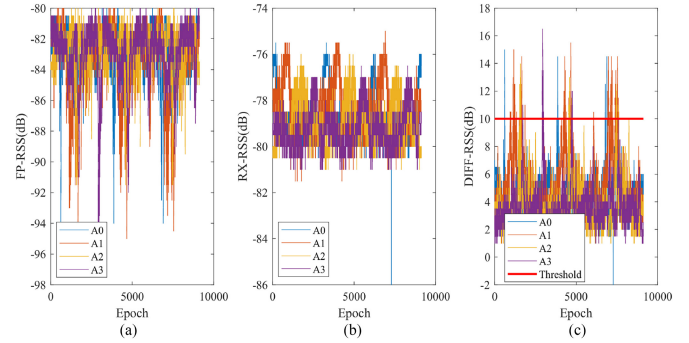


Fig. 24. UWB RSS of four Anchors in Indoor I-3. A0, A1, A2, and A3 denoted UWB anchors. (a) FP component of RSS. (b) Total RSS (RX). (c) RSS difference between the RX and the FP.

algorithm. Figs. 23 and 24 showed the PR and RSS of four anchors in Indoor I-3, respectively.

According to Fig. 24(c), the UWB signal was interfered with by NLOS caused by obstructions, such as tables and chairs, which led to large RSS differences between the total RSS (RX) and FP, e.g., >10 dB. The PRs were deleted if the mutation magnitude was more than an empirical threshold $T_c$.

To present the positioning results more clearly, the positioning trajectories were given in Indoor-I (i.e., the site was covered by one trajectory). The trajectories with and without IM of the HPSs in Indoor I-1 are shown in Figs. 25 and 26. The UWB positioning results displayed mutations in local areas, most probably because of the NLOS impacts.

Overall, the fused UWB+IMU positioning had fewer errors than the UWB itself in the HPS-1 but still deviated from the ground truth in the UWB mutation area. When the same fusion method, e.g., EKF-LC, was applied, the proposed IM algorithm effectively reduced the mutations. The fused trajectories in the UWB mutation area were closer to the ground truth, as shown in the enlarged detailed subfigure. in Figs. 25 and 26. Similar results were obtained in all sensor configurations.

Fig. 27 showed the statistics of the HPS-1 positioning error in Indoor I with and without the IM. The maximum error of the UKF-TC and EKF-TC was 0.445 and 0.558 m, respectively, and the corresponding maximum error with IM was 0.354 and 0.372 m, respectively, i.e., IM was reduced by 21.0% and 33.2% maximum errors. The RMS error of the UKF-TC

and EKF-TC was 0.220 and 0.225 m, respectively, and the corresponding RMS error with IM was 0.207 and 0.204 m, respectively, i.e., IM reduced 6.0% and 9.3% RMS errors. The proposed IM algorithm removed outliers during the positioning process. According to Fig. 27, the average positioning accuracies of the four fusions were almost the same. The positioning accuracy of UKF was slightly higher than that of EKF, and the IM algorithm significantly reduced the positioning maximum error.

The statistics of the HPSs positioning error in Indoor I are shown in Fig. 28. The proposed IM effectively reduced the maximum, mean, and RMS errors in all HPSs. These results indicated that the proposed IM algorithm effectively improved positioning accuracy in proposed HPSs in the indoor experimental scenario.

*2) Outdoor Scene:* The UWB PR and RSS of four anchors in Outdoor I-3 are shown in Figs. 29 and 30, respectively. The UWB PR curve was mostly smooth. Comparing Figs. 29 and 23, the number of PR mutations in Fig. 29 was almost zero as compared to that in Fig. 23. In addition, according to Fig. 30(c), the RSS difference between the RX and the FP had not exceeded 10 dB. This suggested that all anchor channels were in an LOS environment.

The statistics of the HPS-1 positioning error in Outdoor I with and without the IM are shown in Fig. 31.

According to Fig. 31, the positioning accuracy with and without the IM algorithm was almost the same. Since the UWB was in an LOS environment in this experiment, the IM algorithm contributed little to the improvement of positioning accuracy in this case. It can also be seen that the positioning
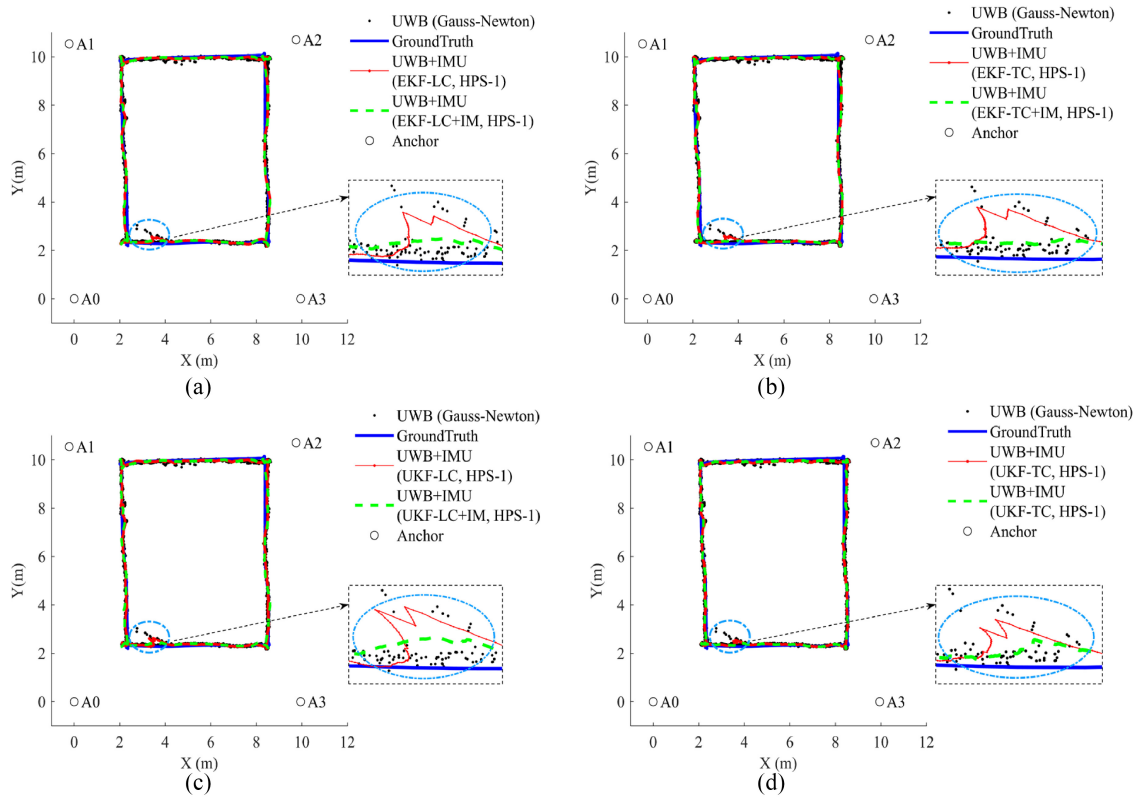
Fig. 25. Trajectories with and without IM of the HPS-1 in Indoor I-1 using four different fusion algorithms. (a) EKF-LC. (b) EKF-TC. (c) UKF-LC. (d) UKF-TC.
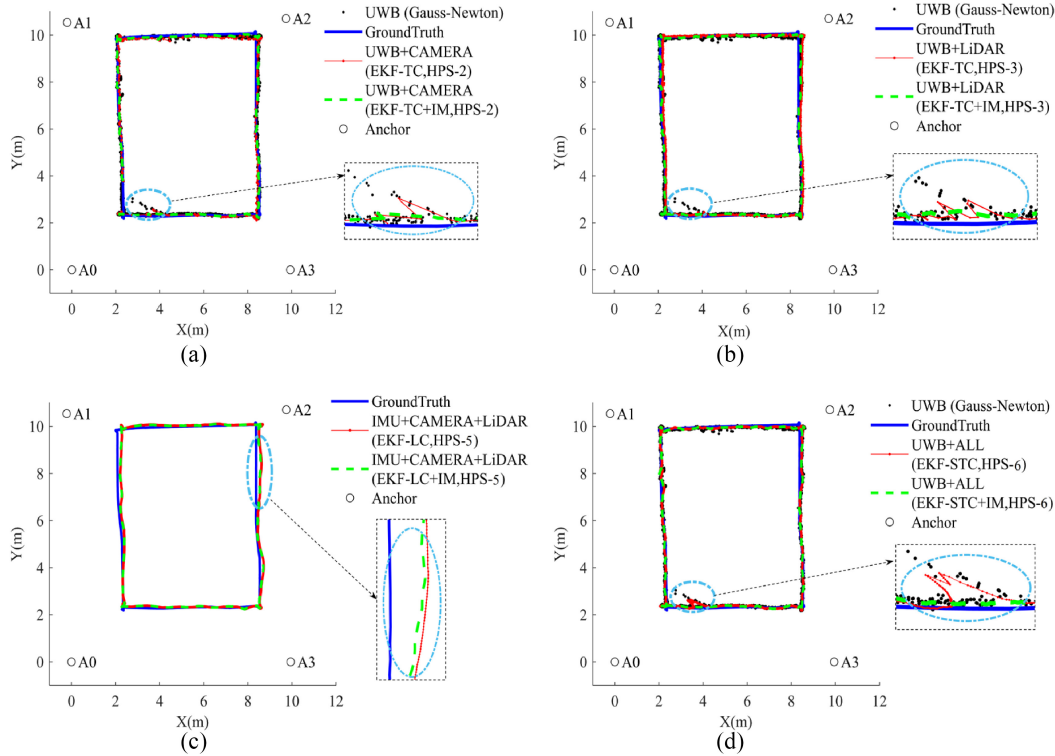


Fig. 26. Trajectories with and without IM of the HPSs in Indoor I-1 using different sensor combinations. (a) HPS-2 (EKF-TC). (b) HPS-3 (EKF-TC). (c) HPS-5 (EKF- LC). (d) HPS-6 (EKF-STC, UWB+ALL represents UWB+IMU+CAMERA+LiDAR.

accuracy of TC is slighter higher than that of LC. In this case, the positioning accuracy of UKF-TC and EKF-TC was almost the same.

### D. Anchor Self-Positioning Results

All experiments performed in the four experimental scenes mentioned above have calculated the positions of anchors using

The HPS-1 positioning error of the Indoor I-1

(a)



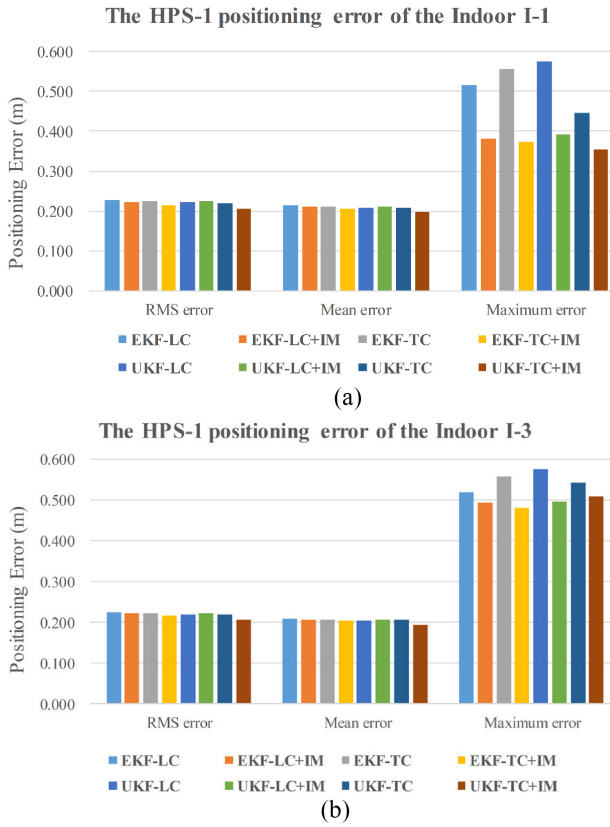The HPS-1 positioning error of the Indoor I-3

(b)

Fig. 27. Statistics of the HPS-1 with and without the IM algorithm in Indoor I, HPS-1 (UWB+IMU). (a) Indoor I-1. (b) Indoor I-3.



The HPSs positioning error of the Indoor I-1

(a)



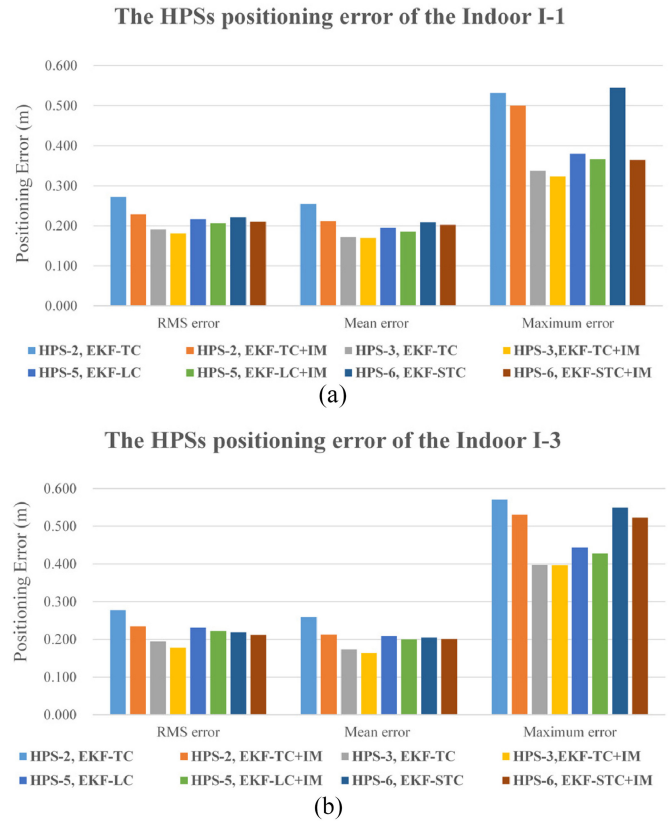The HPSs positioning error of the Indoor I-3

(b)

Fig. 28. Statistics of the HPSs with and without IM algorithm in Indoor I, HPS-2 (UWB+CAMERA+IMU); HPS-3 (UWB+LiDAR); HPS-5 (IMU+CAMERA+LiDAR); HPS-6 (UWB+ IMU+CAMERA+LiDAR). (a) Indoor I-1. (b) Indoor I-3.

the proposed anchor self-positioning algorithm. Without loss of generality, we only present the estimated results and errors of anchor2 (A2) in Outdoor I, as shown in Figs. 32 and 33.

According to Fig. 32, the coordinates of the anchors calculated in the first 30 epochs fluctuate to a certain extent, which was caused by solving the positions of the anchors through the Gauss–Newton iteration. Take the average of the results calculated in the first 30 epochs as the optimal initial value of the EKF-TC estimation, and then estimated the position of the anchors in real-time online. It can be seen from Fig. 33 that for the coordinate estimation of A2 in Outdoor I, within the first 30 epochs, the $z$-coordinate error fluctuated greatly, but the error did not exceed 6.00 cm, and the estimated error of the $x$ and $y$ coordinates was relatively stable within 3.00 cm.

Fig. 34 shows the RMSE of all anchor positions calculated in the different experimental scenarios mentioned above. According to Fig. 34, the maximum RMSE values of the coordinates obtained by the anchor self-positioning were within 7.00 cm, the estimation error of the $z$ coordinate was relatively large, and the error of the $x$ coordinate estimate was the smallest. The average values of the RMSE of all anchor coordinate in the different experimental scenarios calculated by anchor self-positioning proposed in $X, Y$, and $Z$ directions were 1.06, 2.05, and 2.64 cm, respectively. When the initial position of the anchor was given reasonably during initialization, the proposed anchor self-positioning algorithm quickly converged.



(a)



(b)
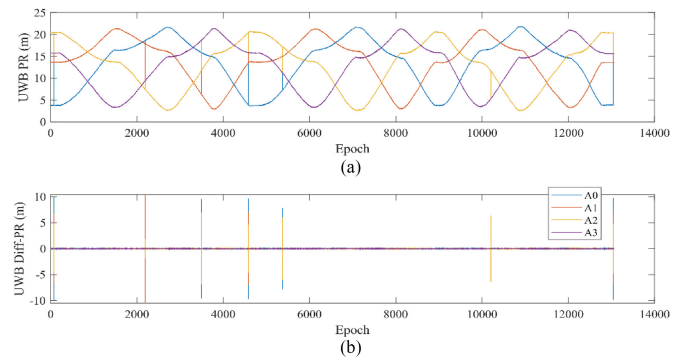
Fig. 29. UWB PRs of four Anchors in the Outdoor I-3. (a) UWB PRs. (b) Difference of the PR between adjacent epochs.

### E. Discussion

According to the experimental results, absolute positioning UWB was quite reliable in an LOS environment. The UWB signals were susceptible to NLOS interference in complex environments, such as indoor scenes, which led to a reduced UWB positioning performance. The experimental results showed that the fusion of ARP effectively corrected the deviation in UWB positioning results caused by NLOS interference.

Relative positioning, i.e., CAMERA+IMU, LIDAR, and RADAR, accumulated errors as the length of the test path increased. Another factor related to error accumulation is the

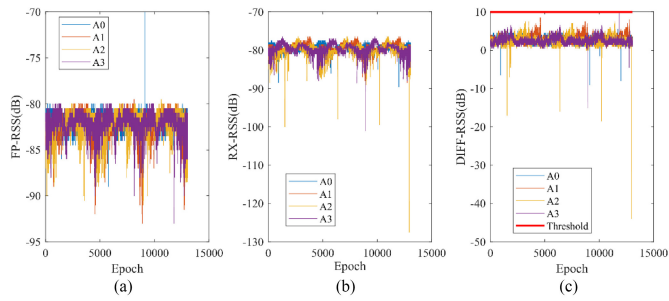Fig. 30. UWB RSS of four Anchors in the Outdoor I-3. A0, A1, A2, and A3 denoted UWB anchors. (a) FP component of RSS. (b) Total RSS (RX). (c) RSS difference between the RX and the FP.
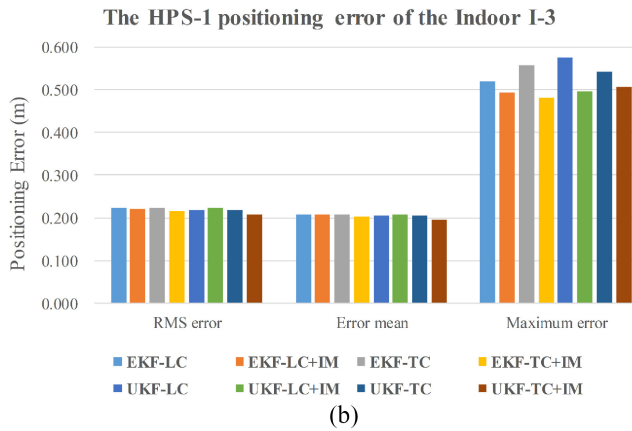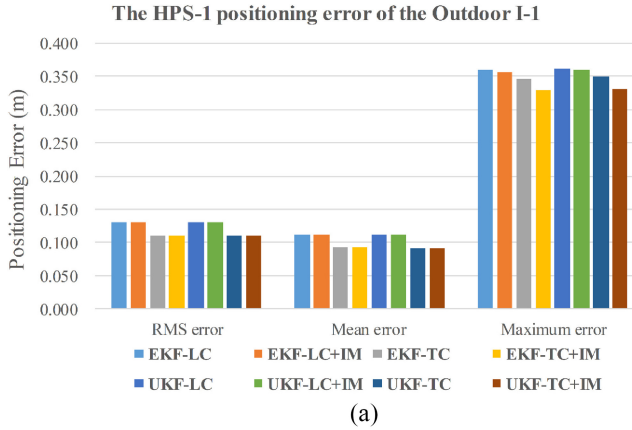


(a)

The HPS-1 positioning error of the Outdoor I-1

(b)

The HPS-1 positioning error of the Indoor I-3

Fig. 31. Statistics of the HPS-1 with and without IM algorithm in Outdoor I, HPS-1 (UWB+IMU). (a) Outdoor I-1. (b) Outdoor I-3.



Fig. 32. Anchor self-positioning results of the A2 in the Outdoor-I within 80 epochs for the (a) X-axis, (b) Y-axis, and (c) Z-axis.
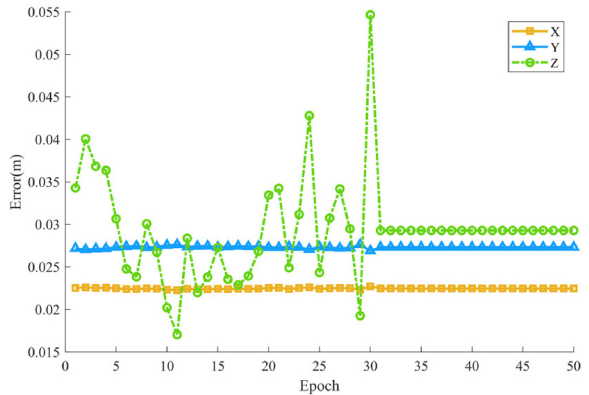


Fig. 33. Anchor self-positioning error of the A2 in Outdoor-I within 50 epochs.
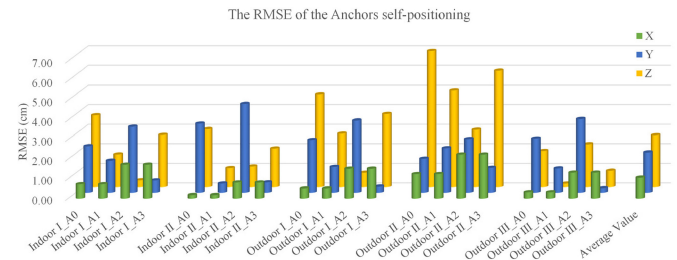


Fig. 34. RMSE of the anchors self-positioning in different experiment scenes.

experimental scene, such as visual texture features, spatial structure, scene size, etc., may have a significant impact on the accuracy of relative positioning. The CAMERA+IMU had a larger error in outdoor open scenes than in Indoor scenes because fewer visual texture features existed in outdoor scenes in the experiments. It did not work in Outdoor III scene because insufficient visual textures existed. RADAR positioning presented the lowest positioning accuracy in all scenes. Among relative positioning, LIDAR showed the most reliable performance in the four in-/outdoor environments.

All six HPSs effectively improved positioning accuracy in comparison with individual positioning technologies alone, i.e., IMU, Camera, LIDAR, and Radar. The average positioning accuracy of the six HPSs reached around 0.200 m

at least, and more than 0.100 m, respectively, in the indoor, and outdoor scenes. The fusion of different positioning solutions effectively reduced the error accumulation over time in relative positioning, especially when large errors existed, such as in camera and RADAR cases.

*1) Positioning Sensors:* UWB can achieve centimeter-level (around 0.100 m) planar positioning accuracy in an LOS environment, given a certain number of anchors, e.g., four in this study. The geometry of UWB anchor networks has a great influence on positioning accuracy. The HDOP simulation showed that the HDOP value was smaller in the middle area of test scenes than in other areas in test scenes when the geometry of four UWB anchors was square in comparison with the rectangle shape. Besides, the smaller the HDOP value, the higher the plane positioning accuracy. This was confirmed

in the field experiments, where Outdoor II has better accuracy than Outdoor I. The maximum, mean, and RMS errors of the UWB were 0.411, 0.113, and 0.157 m in Outdoor I-3, and 0.324, 0.104, and 0.119 m in Outdoor II-3, respectively. In complex environments with obstacles, such as indoors, the NLOS propagation of UWB signals significantly reduces the positioning accuracy.

Relative positioning sensors, i.e., camera, LIDAR, and RADAR, all accumulate positioning errors over time in both indoor and outdoor scenes. The accumulation was much more significant for RADAR, followed by the camera. LIDAR was the most stable and reliable solution of all. The RMSE of the camera, LIDAR, and RADAR positioning ranged from 0.600 to 0.900 m, from 0.100 to 0.250 m, and from 0.900 to 1.700 m, respectively, according to the indoor and outdoor experimental results.

The indoor positioning accuracies of the vision system were higher than that of the outdoor in the experiment. The main reason was that the outdoor environments lack targets or objects. In outdoor scenes with fewer objects/features, e.g., the empty basketball court in Outdoor III, the camera-based visual positioning totally failed, and the RADAR-based positioning was clearly degraded.

RADAR was often used to avoid obstacles or track targets in autonomous driving. This study evaluated the RADAR positioning performances and demonstrated that RADAR-UWB fusion was capable to achieve decimeter-level positioning accuracy.

*2) Fusion Performance:* As of LOS, HPS-1 (UWB+IMU) delivered the highest positioning accuracy in most cases. The RMSE ranged from 0.100 to 0.160 m.

In complex indoor environments where a lot of objects existed as in Indoor I, HPS-3 (UWB+LIDAR) presented the highest positioning accuracy because LIDAR had superior performance to that of UWB. The positioning accuracies of HPS-1, -2, -5, and -6 were almost the same in Indoor I.

In a relatively large-scale open indoor environment, i.e., the underground parking in Indoor II, the positioning accuracy of the six HPSs decreased as follows, i.e., HPS-6 (UWB + IMU + CAMERA + LIDAR) > HPS-1 (UWB + IMU) > HPS-3 (UWB + LIDAR) > HPS-5 (IMU + CAMERA + LIDAR) > HPS-2 (UWB + CAMERA + IMU) > HPS-4 (UWB + RADAR). The number of visual texture features in Indoor II was significantly less than that of Indoor I, resulting in a decrease in the positioning accuracy of the visual positioning. Again, LIDAR was the most reliable solution among all relative positioning solutions.

In an open outdoor case, the positioning performance of HPS-2 (UWB+CAMERA+IMU) was generally lower than that of indoor cases because outdoor scenes possessed fewer texture features. The camera even failed to work in some open outdoor scenes, resulting in no positioning results. Similarly, the indoor positioning accuracy of HPS-4 (UWB+RADAR) and HPS-5 (IMU+CAMERA+LIDAR) was overall higher than that of the outdoors, because of the availability of more features in indoor scenes.

Fusing relative positioning solutions, i.e., HPS-5 (IMU+CAMERA+LIDAR), gave better-positioning results than using UWB alone in both Indoors-I, -II, and Outdoors-II, -III. These results indicated that using the combination of relative positioning sensors can replace the UWB in scenarios where only a local coordinate system was required.

Fusion of absolute positioning using UWB and relative positioning solutions using IMU, CAMERA, and LIDAR, i.e., HPS-6, provided higher positioning accuracy than any ARP alone in most cases, but it did not always deliver the best positioning accuracy in the experimental setups. This suggested that there was a limitation in improving positioning accuracy, such limitation may come from the degraded positioning from a particular component that was typically from the CAMERA and also may come from the used fusion method. This indicates a possible way to improve positioning accuracy for hybrid positioning methods, e.g., the camera information can be abandoned when the system can relay other components for positioning. In this study, the EKF-STC was used to fuse the ARP. The EKF-STC performance required further clarifications in the future.

*3) Fusion Algorithms:* In HPS-1, the overall positioning accuracy of the UKF was slighter higher than that of the EKF in Indoor-I experiments, and the positioning accuracies of UKF and EKF were nearly equal in open outdoor experiments, i.e., the mean error of around 0.080 m. UKF-TC effectively suppressed NLOS and multipath effects in Indoor-I. TC had an overall higher positioning accuracy than that of the LC in the experiments, where TC used the original data of each subsystem to obtain positioning results and could effectively reduce the NLOS effects.

The EKF-TC effectively fused ARP in four HPSs, i.e., HPS-1 (UWB+IMU), HPS-2 (UWB+CAMERA+IMU), HPS-3 (UWB+LIDAR), and HPS-4 (UWB+RADAR). The four HPSs clearly improved the positioning accuracy even though the relative positioning error was relatively large, e.g., CAMERA and RADAR. The results showed that the positioning accuracy of EKF-TC was higher than that of relative and absolute positioning alone.

In HPS-5 (IMU+CAMERA+LIDAR), the positioning accuracy of HPS-5 using EKF-LC was higher than that of UWB alone in most cases and higher than that of LIDAR and CAMERA alone.

The proposed IM algorithm provided two different mechanisms for improving the accuracy and robustness of the UWB-involved HPSs. According to the experimental results, the IM algorithm effectively detected NLOS and removed the positioning outliers during the positioning in indoor scenes, thereby improving the overall positioning accuracy. In outdoor open areas, because of the lack of NLOS conditions in the test site, the IM algorithm did not present clear impacts on positioning accuracy.

The anchor self-positioning algorithm introduced in this study was proven to be effective as shown in experiments. The average 3-D RMSE of the anchor positioning results in the experiments was less than 0.030 m. A reasonable anchor initial value was required that would be more conducive to anchor initialization convergence for the algorithm. The algorithm provided a feasible solution for deployments

of UWB anchors, which has important practical significance in emergency networking applications, such as emergency rescue and crowd evacuation, firefighting, and earthquake relief.

*4) Practical Suggestions for Sensor Selection and Integration in Various Positioning Applications:* HPS-1 integrates UWB and IMU, the positioning accuracy of HPS-1 is at the centimeter level, and it can be used in needed high-accuracy positioning and navigation IoT applications, such as unmanned vehicles and drones.

HPS-2 integrates UWB, CAMERA, and IMU to fully exploit the advantages of each sensor. Camera positioning can provide rich texture information, but positioning accuracy drifts over time, and although the combination of IMU and camera can improve positioning accuracy to some extent, there is still the inherent problem of relative positioning, i.e., positioning errors drifting over time. The UWB can provide centimeter-level positioning, but it does not have texture information, and the positioning accuracy is easily affected by NLOS errors. Thus, HPS-2 can provide a high accuracy and robust positioning system with rich texture information. HPS-2 can be applied to robot navigation in rich texture environments.

HPS-3 integrates UWB and LIDAR. The LIDAR has a more intuitive 3-D representation, robust performance in low-light or texture-less scenes, and can capture details of an environment at a relatively long range. However, the performance of LIDAR positioning significantly deteriorates in large-scale open areas due to limited features. The fusion of the UWB and LIDAR can achieve a high accuracy and robust positioning system. Therefore, the HPS-3 is well suited for applications that require high positioning accuracy but in low-light or texture-less scenes.

HPS-4 integrates UWB and RADAR. The mmWave RADAR is robust for the interference of fog, smoke, dust, and other small particles owing to the longer wavelength. Thus, it is more suitable for hostile environments than the optical camera and LIDAR. The HPS-4 is expected to be able to provide an accurate and robust positioning system in hostile environments (such as fog, smoke, and dust) like firefighting and earthquake.

HPS-5 was realized by integrating the three relative positioning sensors, i.e., IMU, CAMERA, and LiDAR. In some applications where UWB anchors cannot be deployed, it is attempted to combine IMU, CAMERA, and LIDAR to achieve precise and robust positioning solutions.

HPS-6 integrated UWB, IMU, CAMERA, and LIDAR based on the STC, using the complementary advantages of multiple sensors. HPS-6 would be expected to provide an accurate and robust positioning system in cases some positioning sensors may fail in certain environments, e.g., the camera information or positioning results can be a backup solution when other sensors work well and be used as a main positioning solution when other solutions do not function for some reason.

## VI. CONCLUSION

This study benchmarked six hybrid position systems (HPSs) that were based on different integration solutions of five commonly uses ARP technologies, i.e., UWB, IMU, camera, LIDAR, and mmWave RADAR. The six HPSs, i.e., 1) UWB + IMU; 2) UWB + IMU+ camera; 3) UWB + LIDAR; 4) UWB + RADAR; 5) IMU + camera + LIDAR; and 6) UWB+ IMU+ camera + LIDAR, were tested with experiments carried out at four different indoor and outdoor application scenes. A UWB anchor self-positioning algorithm with centimeter-level precision can quickly realize the self-positioning of UWB anchors. This algorithm solved the shortcomings of traditional manual calibration of anchor coordinates, which is time-consuming and labor-consuming. Furthermore, the proposed IM algorithm can detect and eliminate the outliers in the positioning process in time, thereby improving the accuracy and robustness of the positioning system. The performances of the HPSs were rigorously evaluated using millimeter-level ground truth reference that was collected using Leica TS60 total stations.

According to the results of the benchmarking, the RMSEs of the positioning of all proposed HPSs were less than 0.250 m, this verified the effectiveness of the proposed positioning system architecture. In addition, the field experiments also showed that all four algorithms for sensor fusion, i.e., EKF-LC, EKF-TC, UKF-LC, and UKF-TC, can effectively fuse UWB and IMU. The average positioning error was around 0.080 m in the LOS environment. The performance of the TC was slightly superior to that of the LC, and the UKF-TC has a higher positioning accuracy in most cases.

The indoor and outdoor field experiments showed that the accuracy of the IMU, CAMERA, and LIDAR fusion was higher than that of UWB alone in most cases, which indicated the fusion of these relative positioning may replace the use of UWB. For instance, the RMSE of the UWB and IMU+CAMERA+LIDAR was 0.252 and 0.206 m, respectively, in Indoor I-3 experiment. Thus, this fusion solution can be used in applications where it would be inconvenient to deploy UWB infrastructures. Further studies are required to explore more about such applications.

All relative positioning sensors, i.e., camera, LIDAR, and RADAR, accumulated positioning errors over time both in indoor and outdoor scenes. The error accumulation was the most significant for RADAR, followed by the camera. LIDAR, on the contrary, was stable and reliable for relative positioning. In the empty basketball court of Outdoor III scene with few visual objects/features, camera-based visual positioning totally failed; the maximum positioning error of RADAR was 4.661 m in Outdoor III-3, while the maximum error of LIDAR was only 0.541 m.

The positioning accuracy of the fusion of the absolute positioning system UWB and the relative positioning IMU, CAMERA, and LIDAR provided higher positioning accuracy than ARP alone in most cases. However, typically when the camera was involved as a component, the overall performance of the positioning accuracy may be degraded, thus, will lose the competition with other fusion solutions where other sensors were deployed for relative positioning.

The field experimental results also demonstrated that the proposed IM algorithm could effectively detect the NLOS in complex scenes, such as indoor scenes, as well as mitigate

**Algorithm 1** UKF Algorithm

1. Predict update
   Calculate a one-step prediction state vector $\boldsymbol{\xi}_k^-$ of the Sigma sample points:

$$\left(\boldsymbol{\xi}_k^-\right)_i = f\left(\left(\boldsymbol{X}_k^-\right)_i\right) \ (i = 0, 1, \ldots, 2n)$$

   Estimate predicted mean $\widehat{\mathbf{x}}_k^-$ and predicted covariance matrix $\mathbf{P}_k^-$ of the state vector:

$$\widehat{\boldsymbol{x}}_k^- = \sum\nolimits_{i=0}^{2n} \boldsymbol{W}_i^{(m)} (\boldsymbol{\xi}_k^-)_i,$$

$$\mathbf{P}_k^- = \sum\nolimits_{i=0}^{2n} \boldsymbol{W}_i^{(c)} \left[(\boldsymbol{\xi}_k^-)_i - \widehat{\boldsymbol{x}}_k^-\right]\left[(\boldsymbol{\xi}_k^-)_i - \widehat{\boldsymbol{x}}_k^-\right]^T + \boldsymbol{Q}_k.$$

   Predict measurement vector:

$$(\boldsymbol{Z}_k^-)_i = h((\boldsymbol{\xi}_k^-)_i).$$

   Calculate predicted measurement, innovation covariance, and cross-correlation matrix

$$\widehat{\boldsymbol{z}}_k^- = \sum\nolimits_{i=0}^{2n} \boldsymbol{W}_i^{(m)} (\boldsymbol{Z}_k^-)_i,$$

$$\mathbf{P}_{zz} = \sum\nolimits_{i=0}^{2n} \boldsymbol{W}_i^{(c)} \left[(\boldsymbol{Z}_k^-)_i - \widehat{\boldsymbol{z}}_k^-\right]\left[(\boldsymbol{Z}_k^-)_i - \widehat{\boldsymbol{z}}_k^-\right]^T + \mathbf{R}_k,$$

$$\mathbf{P}_{xz} = \sum\nolimits_{i=0}^{2n} \boldsymbol{W}_i^{(c)} [(\boldsymbol{\xi}_k^-)_i - \widehat{\boldsymbol{x}}_k^-][(\boldsymbol{Z}_k^-)_i - \widehat{\boldsymbol{z}}_k^-]^T.$$

2. Measurement update
   Calculate gain matrix $\mathbf{K}_k$.

$$\mathbf{K}_k = \mathbf{P}_{xz}\mathbf{P}_{zz}^{-1},$$

   Update posterior state $\widehat{\mathbf{x}}_k$ and state posterior covariance matrix $\mathbf{P}_k$.

$$\widehat{\boldsymbol{x}}_k = \widehat{\boldsymbol{x}}_k^- + \mathbf{K}_k(\boldsymbol{Z}_k^* - \widehat{\boldsymbol{z}}_k^-)$$

$$\mathbf{P}_k = \mathbf{P}_k^- - \mathbf{K}_k\mathbf{P}_{zz}\mathbf{K}_k^T$$

---

\* $\mathbf{Z}_k$ is the measurement vector. If the fusion method uses TC, the $\mathbf{Z}_k$ shown as in (14), otherwise, $\mathbf{Z}_k$ shown as in (20).

the adverse effect that came from the NLOS conditions, hence improving the overall positioning accuracy of the six HPSs. The proposed anchor self-positioning algorithm effectively solved the problem for the UWB positioning, which generally required measurement of the position of anchors in advance. The anchor self- positioning accuracy was at a centimeter level, which provided a reliable solution to overcome the drawbacks of manually time-consuming measured anchor positions in advance.

In future work, we plan to integrate GNSS positioning into the current benchmark hybrid positioning systems, and further analyze and evaluate the performance using the FGO and filter-based fusion methods, respectively.

## APPENDIX A
## HDOP SIMULATIONS IN FOUR EXPERIMENTAL SCENES

The HDOP simulations and field test ground truth trajectories (Cyan dotted lines) of the experimental scenes were shown in Fig. 35. The smaller the HDOP value, the higher the plane positioning accuracy. As illustrated in Fig. 35, The HDOP value of the four corner positions is greater than that
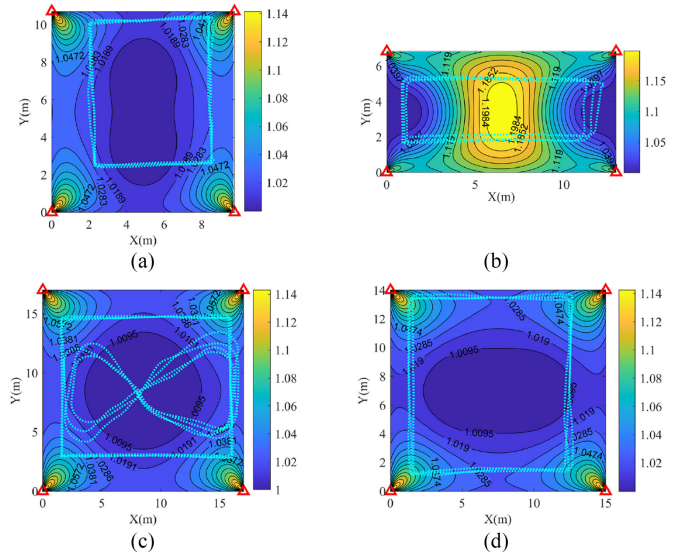


Fig. 35. Simulated result of the HDOP in four experimental scenes. The red triangles represent the UWB-anchor plane positions in field tests. Blue and Yellow represent small and large HDOP values, respectively. Cyan dotted lines represent field test ground truth trajectories. (a) Indoor I. (b) Indoor II. (c) Outdoor I and Outdoor II. (d) Outdoor III.

of the middle area when the positioning area is a square, such as in Fig. 35(a), (c), and (d). The HDOP value of the middle area is the largest when the positioning area is a rectangle, such as in Fig. 35(b). For Indoor II (underground parking) scene, i.e., Fig. 35(b), positioning accuracy in the middle is the worst under the rectangular UWB sensor networks, when other factors that affect the positioning accuracy are the same.

## APPENDIX B
## UWB TAG POSITION ESTIMATION

The UWB tag position $(x, y, z)$ is calculated by multilateration combined with the Gauss–Newton iteration:

$$\begin{cases} (x - x_1)^2 + (y - y_1)^2 + (z - z_1)^2 = d_1{}^2 \\ (x - x_2)^2 + (y - y_2)^2 + (z - z_2)^2 = d_2{}^2 \\ \vdots \\ (x - x_m)^2 + (y - y_m)^2 + (z - z_m)^2 = d_m{}^2. \end{cases} \quad (40)$$

where $(x_1, y_1, z_1), (x_2, y_2, z_2), \ldots, (x_m, y_m, z_m)$ are the anchor coordinates, $d_1, d_2 \ldots d_m$ denote the PRs between the tag and anchors. Linearizing (40) based on the Taylor formula at the initial value $(x^0, y^0, z^0)$, one can get:

$$\mathbf{l} = \mathbf{B}\Delta\boldsymbol{x} + \boldsymbol{\vartheta} \quad (41)$$

$$\mathbf{B} = \begin{bmatrix} \frac{x^0 - x_1}{d_1{}^0} & \frac{y^0 - y_1}{d_1{}^0} & \frac{z^0 - z_1}{d_1{}^0} \\ \vdots & \vdots & \vdots \\ \frac{x^0 - x_m}{d_m{}^0} & \frac{y^0 - y_m}{d_m{}^0} & \frac{z^0 - z_m}{d_m{}^0} \end{bmatrix}$$

$$d_i{}^0 = \sqrt{\left(x^0 - x_m\right)^2 + \left(y^0 - y_m\right)^2 + \left(z^0 - z_m\right)^2}$$

$$(m = 1, 2, \ldots, M) \quad (42)$$

$$\Delta x = \widehat{\boldsymbol{X}} - \boldsymbol{X^0} = \begin{bmatrix} \widehat{x} \\ \widehat{y} \\ \widehat{z} \end{bmatrix} - \begin{bmatrix} x^0 \\ y^0 \\ z^0 \end{bmatrix} \quad (43)$$

$$\mathbf{l} = \boldsymbol{d} - \boldsymbol{d^0} \quad (44)$$

where $\widehat{X}$ is the coordinate estimate of the UWB tag, $\mathbf{B}$ denotes the design matrix. Thus, the correction $\Delta x$ can be calculated based on the least-squares residual squared sum minimum criterion as follows:

$$\Delta \mathbf{x} = \left(\mathbf{B}^T \mathbf{B}\right)^{-1} \mathbf{B}^T l \tag{45}$$

The UWB tag estimate $\widehat{X}$ can be obtained need by iteratively adding the correction $\Delta x$ to the initial estimate, until the correction $\Delta x$ is less than a certain threshold.

## APPENDIX C
### UKF PREDICTION AND MEASUREMENT UPDATE

The prediction and measurement update process of the UKF algorithm is shown in Algorithm 1 after the UT for the system model in Section IV-D2.

## REFERENCES

[1] Y. Zhuang, Q. Wang, M. Shi, P. Cao, L. Qi, and J. Yang, "Low-power centimeter-level localization for indoor mobile robots based on ensemble Kalman smoother using received signal strength," *IEEE Internet Things J.*, vol. 6, no. 4, pp. 6513–6522, Aug. 2019.

[2] X. Liang et al., "*In-situ* measurements from mobile platforms: An emerging approach to address the old challenges associated with forest inventories," *ISPRS J. Photogrammetry Remote Sens.*, vol. 143, pp. 97–107, Sep. 2018.

[3] J. Wang, M. K. Lim, Y. Zhan, and X. Wang, "An intelligent logistics service system for enhancing dispatching operations in an IoT environment," *Transp. Res. E Logist. Transp. Rev.*, vol. 135, Mar 2020, Art. no. 101886.

[4] X. Lu, J. Liu, and H. Zhao, "Collaborative target tracking of IoT heterogeneous nodes," *Measurement*, vol. 147, Dec. 2019, Art. no. 106872.

[5] M. Desai and A. Phadke, "Internet of Things based vehicle monitoring system," in *Proc. Int. Conf. Wireless Opt.*, 2017, pp. 1–3.

[6] A. Sharif et al., "Compact base station antenna based on image theory for UWB/5G RTLS embraced smart parking of driverless cars," *IEEE Access*, vol. 7, pp. 180898–180909, 2019.

[7] Y. Wang et al., "Seamless integration of above- and under-canopy unmanned aerial vehicle laser scanning for forest investigation," *Forest Ecosyst.*, vol. 8, no. 1, p. 10, Feb. 2021.

[8] A. Girma et al., "IoT-enabled autonomous system collaboration for disaster-area management," *IEEE/CAA J. Automatica Sinica*, vol. 7, no. 5, pp. 1249–1262, Sep. 2020.

[9] X. Chen, R. Woogeun, and Z. H. Wang, "Low power sensor design for IoT and mobile healthcare applications," *China Commun.*, vol. 12, no. 5, pp. 42–54, May 2015.

[10] X. Liang et al., "Close-range remote sensing of forests: The state of the art, challenges, and opportunities for systems and data acquisitions," *IEEE Geosci. Remote Sens Mag.*, vol. 10, no. 3, pp. 32–71, Sep. 2022.

[11] I. Balenovic, X. Liang, L. Jurjevic, J. Hyyppa, A. Seletkovic, and A. Kukko, "Hand-held personal laser scanning—Current status and perspectives for forest inventory application," *Croat. J. Forest Eng.*, vol. 42, no. 1, pp. 165–183, 2021.

[12] X. Liang, J. Hyyppa, A. Kukko, H. Kaartinen, A. Jaakkola, and X. Yu, "The use of a mobile laser scanning system for mapping large forest plots," *IEEE Geosci. Remote Sens.*, vol. 11, no. 9, pp. 1504–1508, Sep. 2014.

[13] Z. Liu, L. Chen, X. Zhou, Z. Jiao, G. Guo, and R. Chen, "Machine learning for time-of-arrival estimation with 5G signals in indoor positioning," *IEEE Internet Things J.*, vol. 10, no. 11, pp. 9782–9795, Jun. 2023.

[14] L. Chen, X. Zhou, F. Chen, L.-L. Yang, and R. Chen, "Carrier phase ranging for indoor positioning with 5G NR signals," *IEEE Internet Things J.*, vol. 9, no. 13, pp. 10908–10919, Jul. 2022.

[15] M. Elsanhoury et al., "Precision positioning for smart logistics using ultra-wideband technology-based indoor navigation: A review," *IEEE Access*, vol. 10, pp. 44413–44445, 2022.

[16] Y. Li, Y. Zhuang, P. Zhang, H. Lan, X. Niu, and N. El-Sheimy, "An improved inertial/WiFi/magnetic fusion structure for indoor navigation," *Inf. Fusion*, vol. 34, pp. 101–119, Mar. 2017.

[17] R. Liu, C. Yuen, T. N. Do, M. Zhang, and U. X. Tan, "Cooperative positioning for emergency responders using self IMU and peer-to-peer radios measurements," *Inf. Fusion*, vol. 56, pp. 93–102, Apr. 2020.

[18] H. Yao, H. Shu, X. Liang, H. Yan, and H. Sun, "Integrity monitoring for Bluetooth low energy beacons RSSI based indoor positioning," *IEEE Access*, vol. 8, pp. 215173–215191, 2020.

[19] H. Yao, H. Shu, H. X. Sun, B. G. Mousa, Z. H. Jiao, and Y. B. Suo, "An integrity monitoring algorithm for WiFi/PDR/smartphone-integrated indoor positioning system based on unscented Kalman filter," *EURASIP J. Wireless Commun. Netw.*, vol. 2020, no. 1, p. 246, Dec. 2020.

[20] Q. Fan, B. Sun, Y. Sun, Y. H. Wu, and X. Zhuang, "Data fusion for indoor mobile robot positioning based on tightly coupled INS/UWB," *J. Navig.*, vol. 70, no. 5, pp. 1079–1097, Sep. 2017.

[21] L. Yao, Y. Wu, L. Yao, and Z. Z. Liao, "An integrated IMU and UWB sensor based indoor positioning system," in *Proc. Int. Conf. Indoor Position. Indoor Navigat. (IPIN)*, 2017, pp. 1–8.

[22] Z. Ying, T. Liu, B. Li, Y. Ling, and L. Lou, "Integration of UWB and IMU for precise and continuous indoor positioning," in *Proc. Ubiquitous Position. Indoor Navig. Location Based Services*, 2018, pp. 1–5.

[23] H. Cao, J. Liu, C. Zhu, L. Jing, T. Chen, and T. Wang, "A novel data fusion method for indoor navigation using IMU aided UWB," in *Proc. IEEE 2nd Int. Conf. Electron. Inf. Commun. Technol. (ICEICT)*, 2019, pp. 100–105.

[24] H. Yang, Y. Kuang, M. Wang, X. Bao, and Y. Yang, "Indoor mobile localization based on a tightly coupled UWB/INS integration," in *Proc. 16th Int. Conf. Control Autom. Robot. Vis. (ICARCV)*, 2020, pp. 1354–1359.

[25] W. You, F. Li, L. Q. Liao, and M. L. Huang, "Data fusion of UWB and IMU based on unscented Kalman filter for indoor localization of quadrotor UAV," *IEEE Access*, vol. 8, pp. 64971–64981, 2020.

[26] O. Pohjavirta et al., "Automated registration of wide-baseline point clouds in forests using discrete overlap search," *Forest Ecosyst.*, vol. 9, Jan. 2022, Art. no. 100080.

[27] C. X. Lu et al., "See through smoke: Robust indoor mapping with low-cost mmWave radar," in *Proc. 18th Int. Conf. Mobile Syst. Appl. Services*, 2020, pp. 14–27.

[28] N. El-Sheimy and Y. Li, "Indoor navigation: State of the art and future trends," *Satellite Navig.*, vol. 2, no. 1, p. 7, May 2021.

[29] T. Wang, N. Zheng, J. Xin, and Z. Ma, "Integrating millimeter wave radar with a monocular vision sensor for on-road obstacle detection applications," *Sensors*, vol. 11, no. 9, pp. 8992–9008, Sep. 2011.

[30] Y. Song and L. T. Hsu, "Tightly coupled integrated navigation system via factor graph for UAV indoor localization," *Aerosp. Sci. Technol.*, vol. 108, Jan. 2021, Art. no. 106370.

[31] Leica. "High-performance total station Nova TS60." 2022. [Online]. Available: https://www.directindustry.com/prod/leica-geosystems/product-14324-1205587.html

[32] Y. Song, M. Guan, W. Tay, C. L. Law, and C. Wen, "UWB/LiDAR fusion for cooperative range-only SLAM," in *Proc. Int. Conf. Robot. Autom. (ICRA)*, 2019, pp. 6568–6574.

[33] W. Zhen and S. Scherer, "Estimating the localizability in tunnel-like environments using LiDAR and UWB," in *Proc. IEEE Int. Conf. Robot.*, 2019, pp. 4903–4908.

[34] H. Zhou, Z. Yao, and M. Lu, "Lidar/UWB fusion based SLAM with anti-degeneration capability," *IEEE Trans. Veh. Technol.*, vol. 70, no. 1, pp. 820–830, Jan. 2021.

[35] C. Xu, J. He, X. Zhang, S. Duan, and C. Yao, "3D localization performance evaluation using IMU/TOA fusion methods," *Int. J. Wireless Inf. Netw.*, vol. 26, no. 2, pp. 67–79, Jun. 2019.

[36] Y. Zhang, N. Wang, M. Li, X. Sun, and Z. Wang, "Indoor relative positioning method and experiment based on inertial measurement information/human motion model/UWB combined system," in *Proc. 27th Saint Petersburg Int. Conf. Integr. Navig. Syst. (ICINS)*, 2020, pp. 1–8.

[37] J. D. Hol, F. Dijkstra, H. Luinge, and T. B. Schon, "Tightly coupled UWB/IMU pose estimation," in *Proc. IEEE Int. Conf. Ultra-Wideband (ICUWB)*, 2009, pp. 1–9.

[38] C. Ascher, L. Zwirello, T. Zwick, and G. Trommer, "Integrity monitoring for UWB/INS tightly coupled pedestrian indoor scenarios," in *Proc. Int. Conf. Indoor Position. Indoor Navig. (IPIN)*, 2011, pp. 1–6.

[39] A. Benini, A. Mancini, A. Marinelli, and S. Longhi, "A biased extended kalman filter for indoor localization of a mobile agent using low-cost IMU and UWB wireless sensor network," *IFAC Proc. Vol.*, vol. 45, no. 22, pp. 735–740, 2012.

[40] G. Miraglia, N. Maleki, and L. R. Hook, "Comparison of two sensor data fusion methods in a tightly coupled UWB/IMU 3-D localization system," in *Proc. Int. Conf. Eng. Technol. Innov. (ICE/ITMC)*, 2017, pp. 611–618.

[41] S. Zheng, F. Qiang, H. Tereshchenko, T. Q. Wang, and Q. Quan, "An initial research on ultra-wideband and inertial measurement unit pose estimation for unmanned aerial vehicle," in *Proc. Guid. Navig. Control Conf.*, 2017, pp. 1–9.

[42] D. Feng, C. Wang, C. He, Y. Zhuang, and X. Xia, "Kalman-filter-based integration of IMU and UWB for high-accuracy indoor positioning and navigation," *IEEE Internet Things J.*, vol. 7, no. 4, pp. 3133–3146, Apr. 2020.

[43] S. Lee, B. Kim, H. Kim, R. Ha, and H. Cha, "Inertial sensor-based indoor pedestrian localization with minimum 802.15.4a configuration," *IEEE Trans. Ind. Informat.*, vol. 7, no. 3, pp. 455–466, Aug. 2011.

[44] W. Yan and L. Xin, "The IMU/UWB fusion positioning algorithm based on a particle filter," *Int. J. Geo Inf.*, vol. 6, no. 8, p. 235, 2017.

[45] Q. L. Tian, K. I.-K. Wang, and Z. Salcic, "A low-cost INS and UWB fusion pedestrian tracking system," *IEEE Sensors J.*, vol. 19, no. 10, pp. 3733–3740, May 2019.

[46] S. J. Julier and J. K. Uhlmann, "New extension of the Kalman filter to nonlinear systems," in *Proc. AeroSense*, 1999, pp. 182–193.

[47] P. Vasilyev, S. Pearson, M. El-Gohary, M. Aboy, and J. McNames, "Inertial and time-of-arrival ranging sensor fusion," *Gait Posture*, vol. 54, pp. 1–7, May 2017.

[48] M. Hamer and R. D'Andrea, "Self-calibrating ultra-wideband network supporting multi-robot localization," *IEEE Access*, vol. 6, pp. 22292–22304, 2018.

[49] K. Yu, K. Wen, Y. Li, S. Zhang, and K. Zhang, "A novel NLOS mitigation algorithm for UWB localization in harsh indoor environments," *IEEE Trans. Veh. Technol.*, vol. 68, no. 1, pp. 686–699, Jan. 2018.

[50] Q. Shi, S. H. Zhao, X. W. Cui, M. Q. Lu, and M. D. Jia, "Anchor self-localization algorithm based on UWB ranging and inertial measurements," *Tsinghua Sci. Technol.*, vol. 24, no. 6, pp. 728–737, Dec. 2019.

[51] J. Wang, Y. Gao, Z. Li, X. Meng, and C. M. Hancock, "A tightly-coupled GPS/INS/UWB cooperative positioning sensors system supported by V2I communication," *Sensors*, vol. 16, no. 7, p. 944, Jun. 2016.

[52] B. Ramirez, H. Chung, H. Derhamy, J. Eliasson, and J. C. Barca, "Relative localization with computer vision and UWB range for flying robot formation control," in *Proc. IEEE 14th Int. Conf. Control Autom. Robot. Vis. (ICARCV)*, 2016, pp. 1–6.

[53] Q. Zeng, D. Liu, and C. Lv, "UWB/binocular VO fusion algorithm based on adaptive Kalman filter," *Sensors*, vol. 19, no. 18, p. 4044, Sep. 2019.

[54] G. Ding, H. Lu, J. Bai, and X. Qin, "Development of a high precision UWB/vision-based AGV and control system," in *Proc. IEEE 5th Int. Conf. Control Robot. Eng. (ICCRE)*, 2020, pp. 99–103.

[55] F. Liu, J. Zhang, J. Wang, H. Han, and D. Yang, "An UWB/vision fusion scheme for determining pedestrians' indoor location," *Sensors*, vol. 20, no. 4, p. 1139, 2020.

[56] T. H. Nguyen, T. M. Nguyen, and L. Xie, "Tightly-coupled ultra-wideband-aided monocular visual SLAM with degenerate anchor configurations," *Auton. Robots*, vol. 44, no. 8, pp. 1519–1534, Nov 2020.

[57] A. Sengupta, F. Jin, and S. Cao, "A DNN-LSTM based target tracking approach using mmWave radar and camera sensor fusion," in *Proc. IEEE Naecon. Nat.*, 2019, pp. 688–693.

[58] B. Tan et al., "Improved sensing and positioning via 5G and mmWave radar for airport surveillance," 2022, *arXiv:2202.13650*.

[59] H. Yao, X. Wang, H. Qi, and X. Liang, "Tightly coupled indoor positioning using UWB/mmWave radar/IMU," *Int. Archives Photogrammetry Remote Sens. Spatial Inf. Sci.*, vol. 46, pp. 323–329, Mar. 2022.

[60] A. Kramer, C. Stahoviak, A. Santamaria-Navarro, A. A. Agha-mohammadi, and C. Heckman, "Radar-inertial ego-velocity estimation for visually degraded environments," in *Proc. IEEE Int. Conf. Robot. Autom. (iCRA)*, 2020, pp. 5739–5746.

[61] S. Shioda and K. Shimamura, "Anchor-free localization: Estimation of relative locations of sensors," in *Proc. IEEE Int. Symp. Pers. Indoor Mobile Radio Commun.*, 2013, pp. 2087–2092.

[62] D. Esslinger, M. Oberdorfer, L. Kleckner, O. Sawodny, and C. Tarin, "Receiver self-localization for an opto-acoustic and inertial indoor localization system," in *Proc. IEEE/ASME Int. Conf. Adv. Intell. Mechatron. (AIM)*, 2020, pp. 540–546.

[63] T. H. Nguyen, T. M. Nguyen, and L. H. Xie, "Range-focused fusion of camera-IMU-UWB for accurate and drift-reduced localization," *IEEE Robot. Autom. Lett.*, vol. 6, no. 2, pp. 1678–1685, Apr. 2021.

[64] T.-M. Nguyen, S. Yuan, M. Cao, T. H. Nguyen, and L. Xie, "Viral SLAM: Tightly coupled camera-IMU-UWB-LiDAR SLAM," 2021, *arXiv:2105.03296*.

[65] J. A. Afif, L. K. Seong, and S. Krishnan, "A SVM approach to UWB-IR based positioning under NLOS conditions," in *Proc. IEEE Int. Conf. Commun. Syst.*, 2011, pp. 473–474.

[66] W. Li, T. Zhang, and Q. Zhang, "Experimental researches on an UWB NLOS identification method based on machine learning," in *Proc. IEEE Int. Conf. Commun. Technol.*, 2013, pp. 473–477.

[67] Z. Zeng, S. Liu, and L. Wang, "NLoS identification for UWB based on channel impulse response," in *Proc. IEEE 12th Int. Conf. Signal Process. Commun. Syst. (ICSPCS)*, 2018, pp. 1–6.

[68] G. Zhang, Z. Deng, L. Wen, L. Ge, H. Ke, and J. Jiao, "An UWB location algorithm for indoor NLOS environment," in *Proc. Ubiquitous Position. Indoor Navig. Location Based Services (UPINLBS)*, 2018, pp. 1–6.

[69] C. Jiang, J. Shen, S. Chen, Y. Chen, D. Liu, and Y. M. Bo, "UWB NLOS/LOS classification using deep learning method," *IEEE Commun. Lett.*, vol. 24, no. 10, pp. 2226–2230, Oct. 2020.

[70] X. Li and Y. Wang, "Research on a factor graph-based robust UWB positioning algorithm in NLOS environments," *Telecommun. Syst.*, vol. 76, no. 10, pp. 207–217, 2021.

[71] InvenSense. "MPU-6500 product specification revision 1.3." 2020. [Online]. Available: http://3cfeqx1hf82y3xcoull08ihx-wpengine.netdna-ssl.com/wp-content/uploads/2020/06/PS-MPU-6500A-01-v1.3.pdf

[72] BOSCH. "BMI055 product specification." 2012. [Online]. Available: https://www.bosch-sensortec.com/media/boschsensortec/downloads/product_flyer/bst-bmi055-fl000.pdf

[73] Leica. "Leica geosystems original accessories material Matters." 2019. [Online]. Available: https://pdf.directindustry.com/pdf/leica-geosystems/leica-geosystems-original-accessories-catalogue/14324-671339.html

[74] D. Akopian, A. Melkonyan, and C. L. P. Chen, "Validation of HDOP measure for impact detection in sensor network-based structural health monitoring," *IEEE Sensors J.*, vol. 9, no. 9, pp. 1098–1102, Sep. 2009.

[75] P. G. Savage, "Strapdown inertial navigation integration algorithm design—Part 1: Attitude algorithms," *J. Guid. Control Dyn.*, vol. 21, no. 1, pp. 19–28, Jan./Feb. 1998.

[76] A. Noureldin, T. B. Karamat, and J. Georgy, *Fundamentals of Inertial Navigation, Satellite-Based Positioning and Their Integration*. Heidelberg, Germany: Springer, 2013, ch. 4, pp. 125–166.

[77] X. Niu, T. Liu, J. Kuang, and Y. Li, "A novel position and orientation system for pedestrian indoor mobile mapping system," *IEEE Sensors J.*, vol. 21, no. 2, pp. 2104–2114, Jan. 2021.

[78] L. Chang, X. Niu, T. Y. Liu, J. Tang, and C. Qian, "GNSS/INS/LiDAR-SLAM integrated navigation system based on graph optimization," *Remote Sens.*, vol. 11, no. 9, p. 1009, May 2019.

[79] C. Campos, R. Elvira, J. J. G. Rodriguez, J. M. M. Montiel, and J. D. Tardos, "ORB-SLAM3: An accurate open-source library for visual, visual–inertial, and multimap SLAM," *IEEE Trans. Robot.*, vol. 37, no. 6, pp. 1874–1890, Dec. 2021.

[80] T. Qin. "Advanced implementation of LOAM." 2018. [Online]. Available: https://github.com/HKUST-Aerial-Robotics/A-LOAM

[81] P. Aggarwal, *MEMS-Based Integrated Navigation*. New York, NY, USA: Artech House, 2010.

[82] P. D. Groves, "Principles of GNSS, inertial, and multisensor integrated navigation systems, 2nd edition [book review]," *IEEE Aerosp. Electron. Syst. Mag.*, vol. 30, pp. 26–27, 2015.

[83] G. Panahandeh and M. Jansson, "Vision-aided inertial navigation based on ground plane feature detection," *IEEE/ASME Trans. Mechatronics*, vol. 19, no. 4, pp. 1206–1215, Aug. 2014.

[84] D. Zachariah and M. Jansson, "Self-motion and wind velocity estimation for small-scale UAVs," in *Proc. IEEE Int. Conf. Robot. Autom.*, 2011, pp. 1166–1171.

[85] O. Cetin, H. Nazli, R. Gurcan, H. Ozturk, and H. P. Partal, "An experimental study of high precision TOA based UWB positioning systems," in *Proc. IEEE Int. Conf. Ultra Wideband*, 2012, pp. 357–361.

[86] W. Liu, H. Ding, X. Huang, and Z. Liu, "TOA estimation in IR UWB ranging with energy detection receiver using received signal characteristics," *IEEE Commun. Lett.*, vol. 16, no. 5, pp. 738–741, May 2012.

[87] B. Choi, K. La, and S. Lee, "UWB TDOA/TOA measurement system with wireless time synchronization and simultaneous tag and anchor positioning," in *Proc. IEEE Int. Conf. Comput. Intell. Virtual Environ. Meas. Syst. Appl. (Civemsa)*, 2018, pp. 1–6.

[88] Y. Cheng and T. Zhou, "UWB indoor positioning algorithm based on TDOA technology," in *Proc. IEEE 10th Int. Conf. Inf. Technol. Med. Educ. (ITME)*, 2019, pp. 777–782.

[89] D. Neirynck, E. Luk, and M. Mclaughlin, "An alternative double-sided two-way ranging method," in *Proc. Workshop Position. Naviation Commun.*, 2016, pp. 1–4.

[90] W. Gao, G. Kamath, K. Veeramachaneni, and L. Osadciw, "A particle swarm optimization based multilateration algorithm for UWB sensor network," in *Proc. Conf. Elect. Comput. Eng.*, 2009, pp. 950–953.

[91] Q. Yongyuan, Z. Hongyue, and W. Shuhua, *Kalman Filtering and Integrated Navigation Principles*. Xian, China: Northwestern Polytechn. Univ. Press, 2015.

[92] Y. Yang, "Robust estimation of geodetic datum transformation," *J. Geodesy*, vol. 73, no. 5, pp. 268–274, Jun. 1999.

[93] Y. Yang, M. K. Cheng, C. K. Shum, and B. D. Tapley, "Robust estimation of systematic errors of satellite laser range," *J. Geodesy*, vol. 73, no. 7, pp. 345–349, Aug. 1999.

[94] J. Wang and W. Jian, "Mitigating the effect of multiple outliers on GNSS navigation with M-estimation schemes," in *Proc. IGNSS Symp.*, 2007, p. 9.

[95] Y. Yang, H.-B. He, and G. Xu, "Adaptively robust filtering for kinematic geodetic positioning," *J. Geodesy*, vol. 75, no. 2, pp. 109–116, 2001.

[96] Y. Yang and J. Xu, "GNSS receiver autonomous integrity monitoring (RAIM) algorithm based on robust estimation," *Geodesy Geodyn.*, vol. 7, no. 2, pp. 117–123, Mar. 2016.

**Ruizhi Chen** received the Ph.D. degree from the University of Helsinki, Helsinki, Finland, in 1991.

He is a Full Professor with the State Key Laboratory of Information Engineering in Surveying, Mapping and Remote Sensing, Wuhan University, Wuhan, China. He is a member of the Finnish Academy of Science and Letters. He is committed to the theoretical research and core technology development for seamless indoor/outdoor positioning using smartphones.

**Xiaochen Wang** received the bachelor's degree from Northeastern University, Shenyang, China, in 2019. He is currently pursuing the Ph.D. degree with Wuhan University, Wuhan, China.

His current research interests include LiDAR data processing and simultaneous localization and mapping.
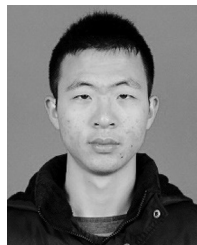
**Hanwen Qi** received the bachelor's and master's degrees from the School of Geodesy and Geomatic, Wuhan University, Wuhan, China, in 2019 and 2021, respectively, where he is currently pursuing the Ph.D. degree.

His research interests include forest point cloud processing and object recognition.

**Haiyun Yao** received the master's degree from the State Key Laboratory of Information Engineering in Surveying, Mapping and Remote Sensing, Wuhan University, Wuhan, China, in 2020, where he is currently pursuing the Ph.D. degree.

His research interests include multi-sensor perception, motion planning, and autonomous exploration for ground and aerial robots.

**Liang Chen** received the Ph.D. degree in signal and information processing from Southeast University, Nanjing, China, in 2009.

He is currently a Professor with the State Key Laboratory of Information Engineering in Surveying, Mapping and Remote Sensing, Wuhan University, Wuhan, China. He has published over 100 scientific articles and five book chapters. His current research interests include indoor positioning, wireless positioning, sensor fusion, and location-based services.

Prof. Chen is currently an Associate Editor of the *Journal of Navigation* and *Navigation-Journal of the Institute of Navigation*.

**Xinlian Liang** (Senior Member, IEEE) received the Ph.D. degree in geoinformatics from Aalto University, Espoo, Finland, in 2013.

He is currently a Full Professor with the State Key Laboratory of Information Engineering in Surveying, Mapping and Remote Sensing, Wuhan University, Wuhan, China. He has published more than 60 SCI papers, including 20 papers as the first/corresponding author. His current research interests include the innovative geospatial solutions in modeling complex environment, including forest ecosystem, from all kinds of point clouds and imagery technologies.
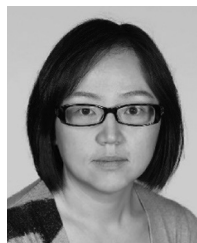
**Yunsheng Wang** received the Ph.D. degree from the University of Freiburg, Freiburg im Breisgau, Germany, in 2008.

She is a Senior Research Scientist from the Department of Remote Sensing and Photogrammetry, Finnish Geospatial Research Institute, National Land Survey of Finland, Helsinki, Finland. Her current research works focus on remote sensing and computational technologies for digitization, reconstruction, and understanding of nature environment (e.g. forest), and studying functioning processes and dynamics in temporal and spatial domains in the context of ecology and climate.

Dr. Wang is the PI and the coPI of several projects funded by the Academy of Finland and EU Horizon 2020. She is the Chair of the ISPRS WG I/7 Data Quality and Benchmark of Sensors, and the Co-Chair of EU COST Action 3DForEcoTech.